

## RESEARCH ARTICLE

10.1002/2016JB012988

## Key Points:

- Frictional properties of Westerly granite at seismic slip rates
- Acoustic emissions during high-velocity friction experiments
- Thermal cracking as a dominant mechanism in wear processes

## Correspondence to:

F. X. Passelègue,  
francois.passelegue@manchester.ac.uk

## Citation:

Passelègue, F. X., E. Spagnuolo, M. Violay, S. Nielsen, G. Di Toro, and A. Schubnel (2016), Frictional evolution, acoustic emissions activity, and off-fault damage in simulated faults sheared at seismic slip rates, *J. Geophys. Res. Solid Earth*, 121, 7490–7513, doi:10.1002/2016JB012988.

Received 11 MAR 2016

Accepted 14 SEP 2016

Accepted article online 19 SEP 2016

Published online 5 OCT 2016

## Frictional evolution, acoustic emissions activity, and off-fault damage in simulated faults sheared at seismic slip rates

François. X. Passelègue<sup>1,2</sup>, Elena Spagnuolo<sup>3</sup>, Marie Violay<sup>4</sup>, Stefan Nielsen<sup>5</sup>, Giulio Di Toro<sup>2,3,6</sup>, and Alexandre Schubnel<sup>1</sup>

<sup>1</sup>Laboratoire de Géologie, CNRS UMR, École Normale Supérieure, Paris, France, <sup>2</sup>School of Earth, Atmospheric and Environmental Science, University of Manchester, Manchester, UK, <sup>3</sup>Istituto Nazionale di Geofisica e Vulcanologia, Rome, Italy, <sup>4</sup>EPFL, LEMR, Lausanne, Switzerland, <sup>5</sup>Department of Earth Science, Durham University, Durham, UK, <sup>6</sup>Dipartimento di Geoscienze, Università Degli Studi di Padova, Padua, Italy

**Abstract** We present a series of high-velocity friction tests conducted on Westerly granite, using the Slow to High Velocity Apparatus (SHIVA) installed at Istituto Nazionale di Geofisica e Vulcanologia Roma with acoustic emissions (AEs) monitored at high frequency (4 MHz). Both atmospheric humidity and pore fluid (water) pressure conditions were tested, under effective normal stress  $\sigma_n^{\text{eff}}$  in the range 5–20 MPa and at target sliding velocities  $V_s$  in the range 0.003–3 m/s. Under atmospheric humidity two consecutive friction drops were observed. The first one is related to flash weakening, and the second one to the formation and growth of a continuous layer of melt in the slip zone. In the presence of fluid, a single drop in friction was observed. Average values of fracture energy are independent of effective normal stress and sliding velocity. However, measurements of elastic wave velocities on the sheared samples suggested that larger damage was induced for  $0.1 < V_s < 0.3$  m/s. This observation is supported by AEs recorded during the test, most of which were detected after the initiation of the second friction drop, once the fault surface temperature was high. Some AEs were detected up to a few seconds after the end of the experiments, indicating thermal rather than mechanical cracking. In addition, the presence of pore water delayed the onset of AEs by cooling effects and by reducing of the heat produced, supporting the link between AEs and the production and diffusion of heat during sliding. Using a thermoelastic crack model developed by Fredrich and Wong (1986), we confirm that damage may be induced by heat diffusion. Indeed, our theoretical results predict accurately the amount of shortening and shortening rate, supporting the idea that gouge production and gouge comminution are in fact largely controlled by thermal cracking. Finally, we discuss the contribution of thermal cracking in the seismic energy balance. In fact, while a dichotomy exists in the literature regarding the partitioning between fracture and heat energy, the experimental evidence reported here suggests that both contribute to fault weakening and off-fault damage.

## 1. Introduction

The energy budget of seismic ruptures is one of the most fundamental questions addressed in seismology as it controls earthquake physics [Scholz, 2002]. It is now accepted that the elastic strain energy released is partitioned into radiated energy at the rupture tip ( $E_r$ ), heat ( $E_h$ ), and fracture energy ( $E_g$ ) during the propagation of the seismic rupture [Abercrombie *et al.*, 2006]. Because earthquakes generally nucleate at depths of several kilometers (i.e., tens to hundreds of MPa) [Oleskevich *et al.*, 1999], most of the current knowledge about the energy budget during earthquakes derives from indirect measurements using inversion methods and interpretation of strong ground motion seismograms and geodetic data or from field investigations along either active or ancient faults. While seismology allows good approximations of  $E_r$  [Haskell, 1964; Boatwright, 1980] and  $E_g$  [Tinti *et al.*, 2005], the estimation of  $E_h$  during earthquakes remains challenging, due to the poor knowledge of the absolute shear stress level. Conversely, field observations allow the estimation of  $E_g$  [Chester *et al.*, 2005; Ma *et al.*, 2006] and  $E_h$ , under the assumptions that fracture and grain size reduction occur mainly during the weakening of faulting and that  $E_r$  is negligible [Chester *et al.*, 2005; Pittarello *et al.*, 2008].

The partition of the energy released during earthquake ruptures can be described by the slip strength history curve [Beeler, 2006]. In the last decades, the advent of high-velocity friction (HVF) apparatus allowed direct measurements of fault strength, with experiments performed close to natural conditions including

displacements comparable to moderate to large in magnitude natural earthquakes [Tsutsumi and Shimamoto, 1997]. The main result of these studies is that faults are expected to become weak during seismic slip, in agreement with seismological and field observations [Brune *et al.*, 1969; Lachenbruch and Sass, 1992]. Fault weakening is explained by the activation of weakening mechanisms generally related to heat production, such as flash heating [Rice, 2006; Goldsby and Tullis, 2011; Passelègue *et al.*, 2014a, 2016; Brantut *et al.*, 2016], melt lubrication [Hirose and Shimamoto, 2005; Di Toro *et al.*, 2006], powder lubrication [Han *et al.*, 2010; Reches and Lockner, 2010], thermal pressurization [Rice, 2006], and thermal decomposition [Han *et al.*, 2007; Brantut *et al.*, 2008, 2016]. In some cases, field evidence supports their occurrence during natural earthquakes [Sibson, 1975; Chester *et al.*, 2005; Hirono *et al.*, 2008; Boullier *et al.*, 2009]. All these mechanisms predict the dramatic reduction of friction coefficient during seismic slip (from static friction  $f_s \approx 0.74$  to dynamic friction coefficient  $f_d \approx 0.1$ ), suggesting very low fault strength during earthquakes.

On the other hand, field studies have shown that fault cores are generally composed of one or more principal slip zones surrounded by an intensely microfractured damage zone [Shipton *et al.*, 2006; Mitchell and Faulkner, 2009; Faulkner *et al.*, 2010, 2011; Fondriest *et al.*, 2012; Passelègue *et al.*, 2014b; Fondriest *et al.*, 2015], believed to be generated by successive seismic events. The creation of damage and plastic strain in fault walls represent energy sinks during earthquake rupture propagation. Damage creation during earthquake rupture, in addition, will induce coseismic variations of the elastic and hydraulic properties of the fault zone (porosity and permeability, for instance), which may be substantial.

The above factors are not well constrained but could play an important role in the earthquake process. Therefore, HVF experiments can be used (i) to analyze the contribution of off-fault damage in the energy balance of earthquakes and (ii) to provide new results about the evolution of physical properties of the fault zone as a function of the final displacement, the sliding velocity, and the initial state of stress.

Here we present friction tests conducted on precut samples of Westerly granite, where the role of coseismic microcracking is investigated with the assistance of acoustic emission (AE) monitoring and the analysis of wave velocity changes in postmortem samples. We first investigated the influence of the effective normal stress and of the sliding velocity on the frictional behavior of the granite, during room humidity and water-saturated experiments under equal effective normal stress. Using a state-of-the-art high-frequency acoustic monitoring system, we monitored the generation of off-fault damage during seismic slip. Second, using a thermoelastic crack model developed by Fredrich and Wong [1986], we demonstrate that heat diffusion can indeed be responsible for substantial damage in the fault walls. The model predicts well both the experimental results and the associated microstructures, suggesting that part of the heat is converted into fracture energy. As a consequence, gouge production and grain size comminution may largely be controlled by thermal cracking at least in granitic rocks. Finally, we show that thermal cracking induced during seismic slip, under room humidity conditions, controls the evolution of the physical properties of the slip zone and the high-frequency radiation.

## 2. Methods

### 2.1. Sample Preparation

All experiments were conducted on precut samples of Westerly granite by shearing two hollow cylinders of 30/50 mm internal/external diameter. The internal concentric hole presented a depth of 7 mm to maintain the propagation of waves in the sample toward acoustic sensors. The half length of the sample assemblage was about 5 cm. The fault surface was smoothed using a surface grinder to impose a constant roughness (wavelength of  $\approx 50 \mu\text{m}$  and height of  $\approx 10 \mu\text{m}$ ) on all sample assemblages.

### 2.2. SHIVA

Experiments were conducted on SHIVA (Slow to High Velocity Apparatus) at the Istituto Nazionale di Geofisica e Vulcanologia (INGV-Rome). The rotary shear apparatus uses two brushless motors to supply the torque (shear stress), the angular rotation, and nominally infinite slip. Thanks to the large power available (300 kW), SHIVA can impose realistic seismic deformation conditions in terms of normal stress, velocity, and acceleration up to 50 MPa for standard 30/50 mm internal/external diameter,  $6.5 \text{ m s}^{-1}$ , and  $65 \text{ m s}^{-2}$ , respectively. Normal force is applied to the sample via an air-actuated intensifier (Figure 1a) acting through an arm to amplify the resulting normal force.

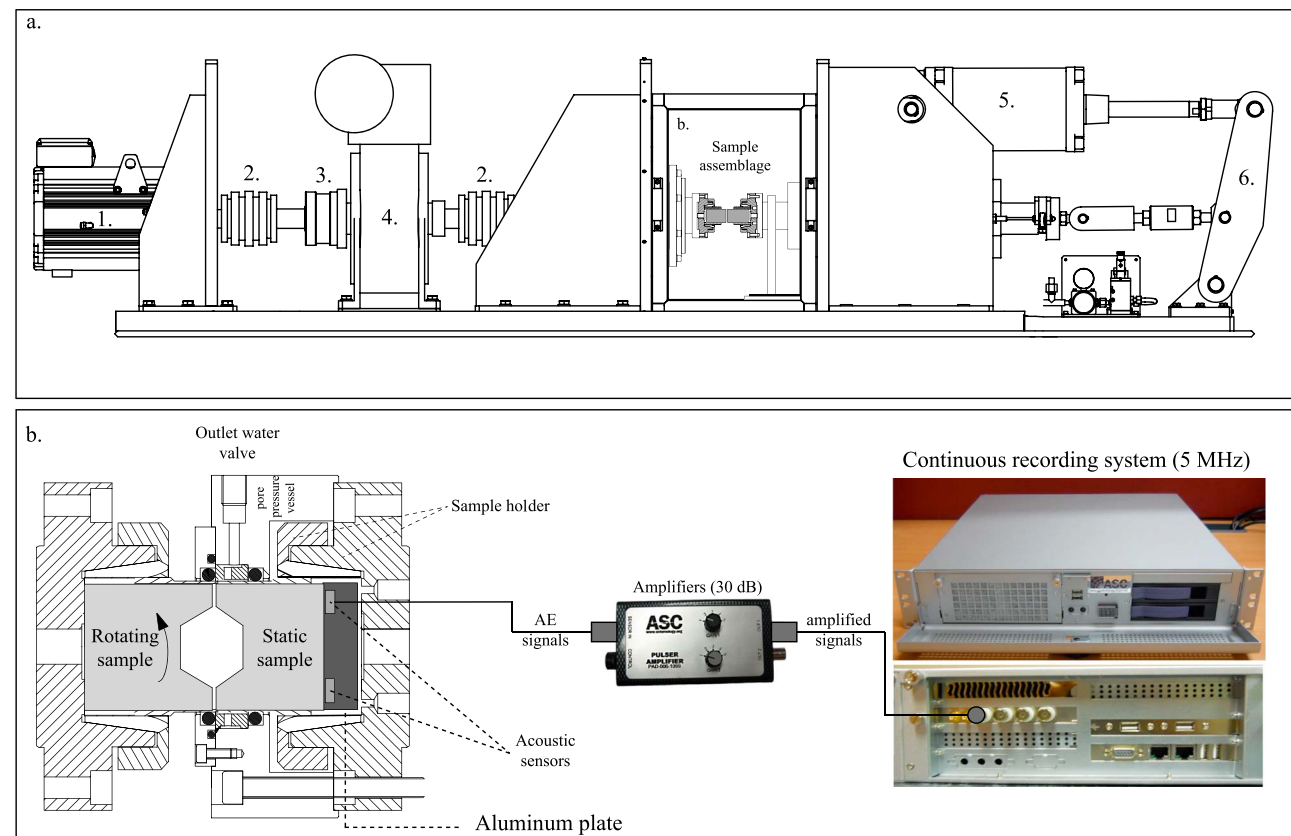


**Figure 1.** Slow to High Velocity Apparatus. (a) 1. Large electric motor. 2. Bellow couplings. 3. Sprag clutch. 4. Gear box. 5. Air actuator. 6. Steel arm to amplify the axial load. The axial load is imposed by the air actuator and monitored by a computer. The torque is measured using a torque bar. (b) Experimental configuration and description of the sample holder, the fluid pressure system, and the high-frequency monitoring system. Experimental pore fluid system consists of a liquid fluid pressure vessel, a membrane pump, a pressure multiplier, and a pressure regulator [Violay et al., 2013]. Shear wave sensors were used in this study. These sensors also allow recording of the *P* wave arrival during experiments. The signal is amplified at 45 dB (i.e., \*177 the amplitude of the real signal). The Richter ASC system is used to record the continuous acoustic waveforms during experiments.

The angular rotation velocity of the rock sample is measured by two digital and optical encoders located in the rotary column [see Niemeijer et al., 2011]. The average sliding velocity or equivalent velocity ( $V_e$ ) is then estimated following [Tsutsumi and Shimamoto, 1997]

$$V_e = \frac{2R(r_{\text{ext}}^2 + r_{\text{int}}r_{\text{ext}} + r_{\text{int}}^2)}{3(r_{\text{int}} + r_{\text{ext}})} \quad (1)$$

where  $R$  is the angular speed,  $r_{\text{int}}$  is the internal radius of the rock sample (here 15 mm), and  $r_{\text{ext}}$  is the external radius of the sample (here 25 cm). The upkeep of the axial column is assured by a 50 cm long arm attached to the concrete base through a vertical steel bar (Figure 1a).

The torque was measured using an S beam-type load cell (operating in extension) which can go up to 3 kN with a resolution of 3 N. The load cell is located at the lower end of the vertical bar (Figure 1a). The conversion of torque into shear stress is approximated using [Hirose and Shimamoto, 2005]

$$\text{Torque} = 2\pi\tau \int_{r_{\text{int}}}^{r_{\text{ext}}} r^2 dr \quad (2)$$

where  $r$  is the radius of the cylindrical specimens, assuming that shear stress  $\tau$  is constant over the fault surface.

Shortening of the sample during experiments was measured via a spring-loaded Diameter Variable Differential Transformer (DVDT) position sensor located behind the rigid arm and by a Linear Variable Differential Transformer (LVDT) located in the sample chamber close to the sample. DVDT has a full-scale range of 50 mm with a resolution of 50  $\mu\text{m}$ , while the LVDT has a full-scale range of 3 mm with a resolution of 300 nm. Mechanical data including axial load, torque, axial shortening, and angular rotation were acquired at a sampling rate up to 25 kHz. Further details can be found in Di Toro et al. [2010] and Niemeijer et al. [2011].

### 2.3. Fluid Vessel

To perform experiments in the presence of water, SHIVA is equipped with a pressurizing system [Violay *et al.*, 2013] which consists of a pore fluid pressure vessel (Figure 1b) allowing sample saturation with pressurized fluids, a membrane pump with a  $30\text{ cm}^3$  fluid capacity, and a pressure intensifier that imposes up to 15 MPa of fluid pressure on the fault surface (Figure 1b). Once the chosen fluid pressure is reached, the effective normal stress is increased until the chosen target. The fluid pressure sensor is located at about 5 mm from the fault surfaces but still allows the measurement of pressure changes during experiments, for example the pressurization resulting from thermal frictional heating of the sliding interface, as reported in a previous study [Violay *et al.*, 2015].

### 2.4. Acoustic Emission Setup

Acoustic transducers used in this study are piezoceramic shear plates, which consist of a PieZoelectric transducer crystal (PI ceramic Pi255,  $5 \times 5\text{ mm}$  and  $0.5\text{ mm}$  thick), encased within an aluminum holder, directly glued at the bottom part of the static sample using a custom-designed transducer holder (Figure 1b). The piezo-electric crystals are all transversely polarized the same way and record preferentially shear waves. Signals are amplified at 45 dB and then relayed via coaxial cables to a four-channel digital oscilloscope, which allows for continuous recording on four channels at 10 MHz (Richter minisystem, ASC Ltd.). Theoretically, the system has no limit in event triggering, and all the events can be recorded. Continuous waveforms are then processed via a software (Insite, ASC Ltd.) to be harvested into discrete acoustic emission (AE) events. The harvesting is performed following a trigger logic, i.e., a given amplitude threshold on a given number of channels within a given time window. Typically, the downtime (i.e., minimum interevent time between two consecutive harvested AEs) is set at 200 ms (typical length of an AE signal), in order not to harvest an event twice, so that, in this setup, maximum AE recording rate is of the order of 5000/s.

## 3. Experimental Results

### 3.1. Typical Frictional Behavior Under Room Humidity Conditions

Room humidity experiments were conducted at 5, 10, and 20 MPa of effective normal stress  $\sigma_n^{\text{eff}}$  and at 0.003, 0.03, 0.1, 0.3, 1, and 3 m/s of target sliding velocity  $V_s$  (Table 1). We first compare the influence of the sliding velocity on the frictional behavior of the experimental fault. In all experiments, the effective friction coefficient ( $\tau/\sigma_n^{\text{eff}}$ ) first increases linearly with displacement up to values corresponding to typical static friction coefficient ( $f_s \approx 0.7$ ) [Byerlee, 1978], during the very initial acceleration part of the slip history (Figure 2). After that, the frictional behavior is a function of the instantaneous sliding velocity ( $V_s$ ) and ambient conditions (Figure 2b).

At low sliding velocity (from 0.003 to 0.03 m/s) and room humidity conditions, after achieving quasi-static values  $f_s$ , the friction coefficient continuously decreases to 0.65 with slip (Figure 2a). The friction coefficient is quite variable during low-velocity experiments. In this velocity range, the slip-weakening distance to steady state  $D_{ss}$ , corresponding to the amount of slip required to reach the energetic equilibrium in the slipping zone and wall rocks [Nielsen *et al.*, 2008], is hard to define because the steady state friction coefficient may not be achieved. In this case, the value of  $D_{ss}$  corresponds to the achievement of a minimum friction coefficient.

At seismic sliding velocities (from 0.1 to 3 m/s), the frictional behavior of the simulated fault presents systematic characteristics. At the beginning of the sliding, i.e., during the acceleration part of the slip history, the friction coefficient increases up to static values ( $f_s \approx 0.7$ ). Then, the friction coefficient decreases after a few centimeters of slip, down to a critical value defined as  $f_w \approx 0.35$  (Figure 2b). The initial weakening is followed by frictional strengthening, highlighted by a second peak of strength, noted as  $f_p$ . Once  $f_p$  is overcome, the friction coefficient decreases with increasing slip as observed in previous studies [Tsutsumi and Shimamoto, 1997; Hirose and Shimamoto, 2005], and a large weakening is observed until the friction coefficient reaches a steady state value ( $f_{ss}$ ) (Figure 2b). The steady state condition is achieved when the amount of slip becomes greater than a slip-weakening distance  $D_{ss}$ . Frictional parameters inferred from experiments are presented in Table 2.

Water-saturated experiments exhibit a different behavior and will be discussed later.

### 3.2. Influence of Sliding Velocity on AE Activity

The mechanical behavior is now compared to AE activity for experiments conducted at different sliding velocities but under similar effective normal stress conditions ( $\sigma_n^{\text{eff}} = 10\text{ MPa}$ ) (Figure 3). At low sliding velocity

**Table 1.** High-Velocity Experiments Discussed Here<sup>a</sup>

Experiments	$\sigma_n^{\text{eff}}$ (MPa)	$P_f$ (MPa)	$V_s$ (m/s)	Shortening (mm)	Slip (m)
s656	10	-	0.003	0.18	1.00
s658	5	-	0.3	2.51	5.61
s662	10	-	0.3	3.04	2.94
s663	20	-	0.03	0.24	1
s664	20	-	0.3	3.06	3.27
s666	10	-	3	2.83	5.00
s675	20	-	3	3.31	3.43
s676	20	-	1	5.18	7.54
s843	10	-	0.1	1.75	2.00
s844	20	-	0.1	2.28	1.69
s845	10	-	1	2.64	4.09
s849	20	-	0.3	2.39	1.88
s850	10	5	0.3	0.79	3.96
s851	10	5	0.3	0.6	3.59
s852	10	-	0.3	1.77	1.00
s853	10	-	3	3.21	4.09

<sup>a</sup>All experiments have been conducted on Westerly granite.  $\sigma_n^{\text{eff}}$  = effective normal stress,  $P_f$  = fluid pressure,  $V_s$  = target sliding velocity. The shortening and the slip correspond to final values.

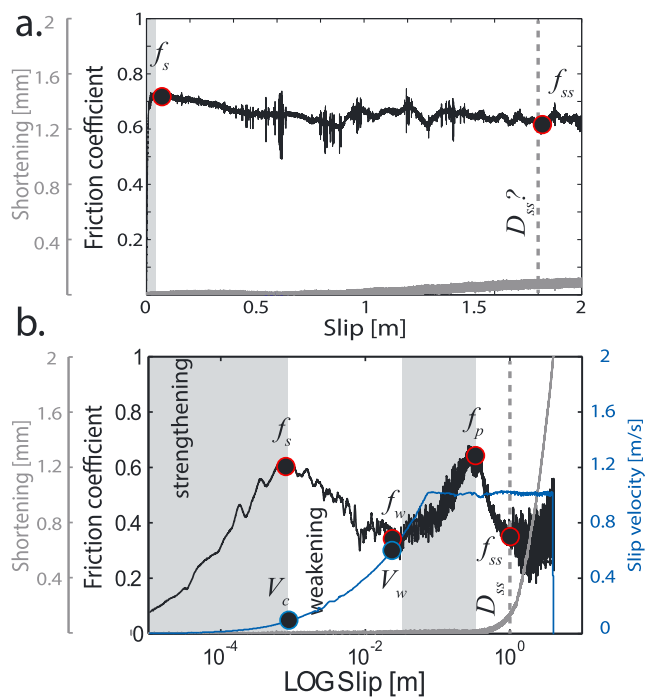


**Figure 2.** Friction coefficient and shortening evolution with slip during experiments performed under room humidity conditions. (a) Experiment s656 preformed at  $\sigma_n^{\text{eff}} = 10$  MPa and  $V_s = 0.003$  m/s. The friction coefficient increases up to typical static values [Byerlee, 1978]. Then, the friction coefficient weakens up to the end of the experiments. (b) Experiment s845 preformed at  $\sigma_n^{\text{eff}} = 10$  MPa and  $V_s = 1$  m/s. The friction coefficient is plotted with log slip to illustrate better the weakening and strengthening steps observed at the initiation of the slip. These results are comparable to those obtained on India gabbro [Tsutsumi and Shimamoto, 1997; Hirose and Shimamoto, 2005].

**Table 2.** Frictional Parameters Inferred From Experiments<sup>a</sup>

Experiments	$f_s$	$f_w$	$f_p$	$f_{ss}$	$V_c$ (m/s)	$V_w$ (m/s)	$D_{ss}$ (m)
s656	-	-	0.72	0.61	-	-	-
s658	0.63	0.45	0.78	0.36	0.096	0.16	2.30
s662	0.82	0.41	0.76	0.26	0.12	0.29	0.87
s663	-	-	0.86	0.65	-	-	-
s664	0.61	0.39	0.59	0.30	0.077	0.22	0.80
s666	0.59	0.27	0.65	0.33	0.10	0.89	0.75
s675	0.57	0.24	0.56	0.17	0.09	0.63	0.67
s676	0.60	0.23	0.54	0.14	0.08	0.86	0.86
s843	0.81	0.51	0.83	0.31	0.09	0.010	1.97
s844	-	-	0.75	0.25	-	-	1.38
s845	0.62	0.33	0.75	0.38	0.11	0.51	1.12
s849	0.67	0.33	0.56	0.19	0.10	0.29	0.96
s850	-	-	0.42	0.11	-	-	1.97
s851	-	-	0.42	0.12	-	-	2.17
s852	0.64	0.38	0.76	0.22	0.09	0.30	0.74
s853	0.61	0.28	0.66	0.37	0.13	0.67	0.78

<sup>a</sup>List of the different mechanical parameters deduced from experiments.  $f_s$  = quasi-static friction coefficient at the onset of slip,  $f_w$  = friction coefficient at the first weakening,  $f_p$  = friction coefficient at the second peak of strength,  $f_{ss}$  = the steady state friction coefficient,  $V_c$  = sliding velocity at which the first weakening starts,  $V_w$  = sliding velocity at which  $f_w$  is achieved,  $D_{ss}$  = amount of slip for which  $f_{ss}$  is reached.

( $V_s = 0.003$  m/s), the AE activity is irregular. For some slip and time intervals, the experimental fault remains silent, while during other intervals, bursts of AEs are observed. However, no evident correlation between AE activity and frictional behavior can be determined (Figure 3a). The increase of slip along the fault seems, however, to increase the AE activity, at least for low-amplitude AE (amplitude < 0.5 V).

At  $V_s = 0.1$  m/s, an intense AE activity is observed at the beginning of the sliding. Then the friction coefficient increases up to  $f_p$ . During this strengthening step, the AE activity is irregular, with a small increase in intensity with slip. Once  $f_p$  is overcome, strong variations of friction coefficient are observed for about 1 m of slip. Friction coefficient drops are generally correlated with a release of AEs (Figure 3b). When friction increases, less AEs are recorded. After  $\approx 1.8$  m of slip, the friction coefficient reaches the steady state value  $f_{ss}$ . This sharp decrease of the friction coefficient corresponds to the initiation of the shortening of the sample and is associated with a strong increase of the number of AEs detected.

At higher slip rate ( $V_s > 1$  m/s), AEs are mainly observed once  $f_{ss}$  is achieved (Figure 3c). The AE activity decreases during the first weakening, but a small increase of the AE activity is observed during the strengthening part (up to  $f = f_p$ ). During the second weakening step (from  $f_p$  to  $f_{ss}$ ), an increase of AE activity is observed up to the end of the experiment, concomitant with the large increase in the shortening rate of the sample. A similar behavior is observed for experiments conducted at 3 m/s slip rate. Most of the AEs are generated once the friction coefficient reaches  $f_{ss}$ , i.e., during the second part of the experiments (Figures 3b and 3c).

At high sliding velocities ( $V_s \geq 0.3$  m/s), high-amplitude AEs are recorded a few seconds after the end of the sliding step, while the length of the sample remains constant (Figure 3c).

### 3.3. Influence of Effective Normal Stress and Effective Pressure on AE Activity

Figure 4 presents the result of three experiments conducted under different effective normal stress and ambient conditions. The first experiment presented (Figure 4a) was conducted at  $V_s = 0.3$  m/s and  $\sigma_n^{\text{eff}} = 10$  MPa under room humidity conditions. AE activity decreases within the friction coefficient during the first weakening (when  $f$  decreases from  $f_s$  down to  $f_w$ ). During the strengthening part, when  $f$  increases up to  $f_p$ , a small increase of the AE activity is observed. As during the experiments conducted at 0.1 m/s (Figure 3b), a strong

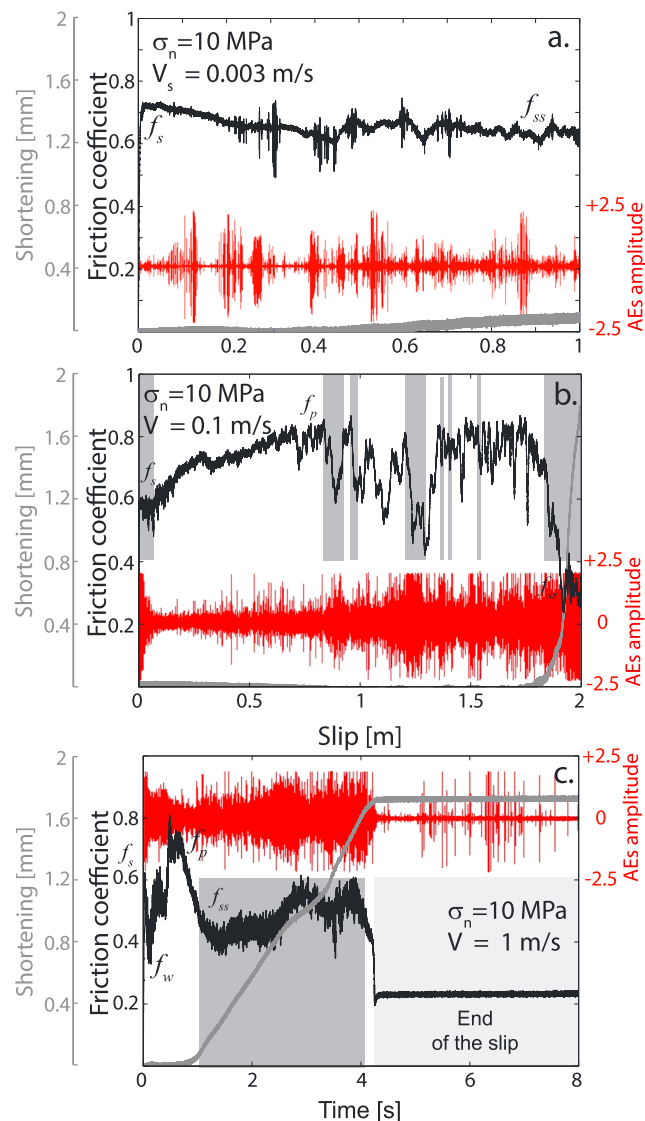


**Figure 3.** Evolution of the friction coefficient, the shortening, and the AE activity during experiments (a) s656, (b) s843, and (c) s845, conducted at 0.003, 0.1, and 1 m/s, respectively. All experiments were conducted at 10 MPa effective normal stress and room humidity conditions. The AE activity after the end of sliding step of the experiment conducted at  $\sigma_n^{\text{eff}} = 10 \text{ MPa}$  and  $V_s = 1 \text{ m/s}$  is presented in Figure 3c.

increase of the AE activity is observed when the slip reaches  $D_{ss}$ , which is correlated with the initiation of large shortening. From this slip distance, the amplitude of the acoustic waveforms saturate up to the end of the experiment.

Under higher effective normal stress ( $\sigma_n^{\text{eff}} = 204 \text{ MPa}$ ), a similar behavior is observed. Doubling the effective normal stress acting on the fault surface does not have a strong influence on the AE intensity. The AE activity increases from the second peak of strength  $f_p$  up to the end of the experiments (Figure 4b). The peak of AE intensities is observed when the shortening rate is maximum (i.e., between 3 and 4.5 s or 0.9 and 1.4 m of slip in Figure 4b).

The water-saturated experiments exhibit a different behavior. The first weakening is not observed, and the friction coefficient decreases almost linearly with displacement down to  $f_{ss}$  (Figure 4c). However, the static friction coefficient is much smaller than in room humidity conditions ( $f_s \approx 0.4$ ). In addition, few AEs are detected, which correlates with the negligible shortening in the first 5 s (corresponding to 1.5 m of slip). When evident shortening starts, we do not observe a strong increase in the AE activity (Figure 4c). Given the same effective

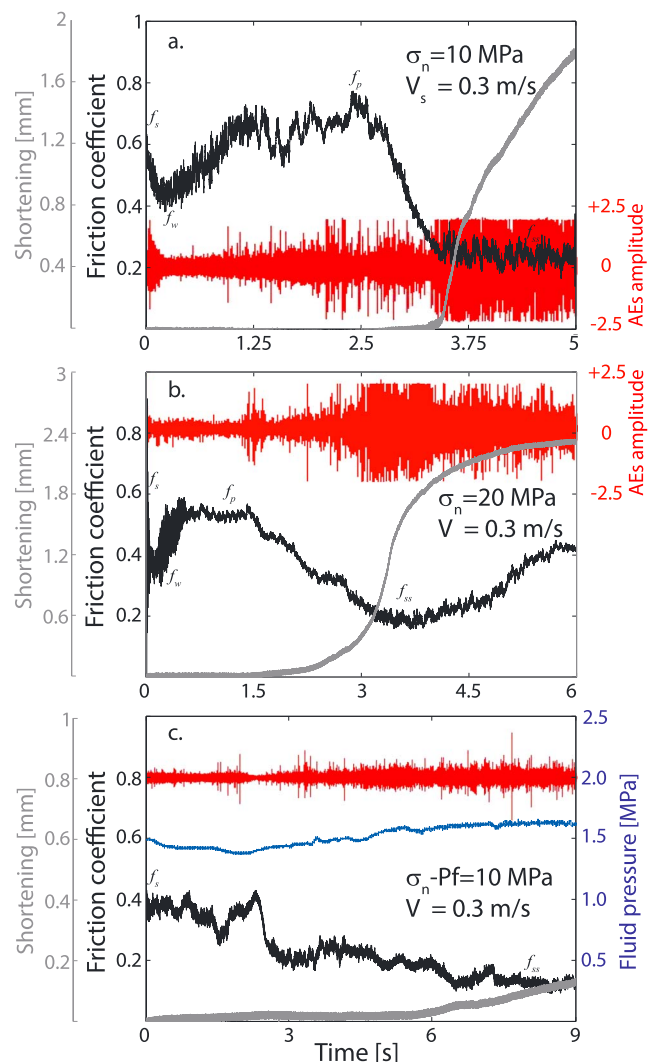


**Figure 4.** Influence of effective stress for three experiments conducted at 0.3 m/s. (a) Experiment s852 conducted at 10 MPa effective normal stress and room humidity conditions. (b) Experiment s849 conducted at 20 MPa effective normal stress and room humidity conditions. Experiment s851 conducted in water-saturated conditions ( $\sigma_n^{\text{eff}} = 10 \text{ MPa}$ ).

normal stress, velocity, and slip (1.2 m), the total sample shortening is  $\approx 1.6 \text{ mm}$  in the room humidity experiment and only  $\approx 0.05 \text{ mm}$  in the water-saturated experiment. These results suggest that the presence of water in the sliding zone reduces the number of AE and the amount of shortening. Note that the fluid pressure, measured very close to the fault plane, remains constant during the entire experiment (Figure 4c), suggesting that thermal pressurization does not occur during this experiment.

### 3.4. Elastic Wave Velocity Measurements

After each experiment, P and S wave velocities (respectively,  $C_p$  and  $C_s$ ) were measured on both samples (static and rotating rock cylinders) using commercial acoustic sensors. The  $C_p$  and  $C_s$  measurements are a good proxy to estimate off-fault damage induced during experiments, because P and S wave velocities are sensitive to the presence of cracks in the medium and both velocities are supposed to decrease with the crack density  $\rho_{\text{cr}}$  [Walsh, 1965]. The measurements were conducted a few days after the experiments, at room pressure and temperature conditions. Samples were previously dried for 24 h at 60°C. During experiments, damages are expected to be localized close to the fault surface. Therefore, both P and S waves were transmitted through the entire sample because of the frequency response of the sensors ( $\approx 500 \text{ kHz}$ ). Because waves travel in the slipping zone but also in intact granite during measurement, wave velocities measured correspond to average values.

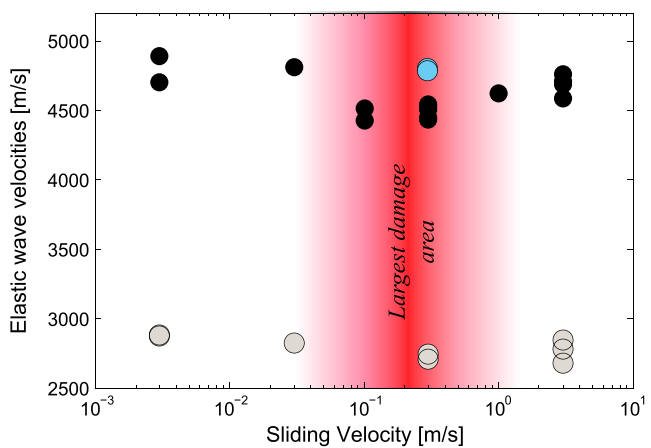


**Figure 5.** Measurements of  $P$  and  $S$  wave velocities in postmortem samples as a function of the sliding velocity imposed during each experiment. Black and grey circles correspond, respectively, to  $P$  and  $S$  wave velocity measurements. Blue circles correspond to experiments conducted in the presence of water. The red area highlights sliding velocities inducing the highest off-fault damage. The error bars are smaller than the marker's size.

Below 0.01 m/s, there is no change in wave velocities in comparison to intact Westerly granite (Figure 5). However, a decrease in both  $C_p$  and  $C_s$  is observed at higher sliding velocities. The smaller velocity values are observed for  $V_s = 0.3$  m/s, while only a small velocity decrease is observed at  $V_s = 3$  m/s (Figure 5). These results suggest that more damage is induced in the rock sample (close or at a distance to the fault plane) for this critical range of sliding velocities. However, no strong correlation between damage and  $\sigma_n^{\text{eff}}$  is observed. The variation of damage due to  $\sigma_n^{\text{eff}}$  is generally negligible compared to the influence of  $V_s$ .

The measurements of  $C_p$  and  $C_s$  conducted in postmortem samples of water-saturated experiments ( $\sigma_n^{\text{eff}} = 10$  MPa and  $V_s = 0.3$  m/s) show negligible variation of elastic wave velocities in comparison with measurements performed on intact rocks. These results suggest that the presence of water inhibits damage during high-velocity frictional experiments, as already suggested by the small amount of AEs and shortening recorded during these experiments (Figure 4).

## 4. Microstructural Observations

### 4.1. State of the Slipping Zone With Increasing Slip

To study the microstructures at the different weakening steps, we conducted three dedicated experiments at 0.3 m/s slip rate and 10 MPa effective normal stress. We stopped the experiments at three given characteristic displacements (0.015, 0.5, and 1.5 m of slip), which correspond, respectively, to the first weakening ( $f_w$ ), the initiation of the second weakening ( $f_p$ ), and the steady state friction coefficient ( $f = f_{ss}$  and  $D > D_{ss}$ ) (Figure 6a). Optical and scanning electron microscopy were conducted on postmortem samples for microstructural analysis.

The state of the fault surface at the first weakening, when  $f = f_w$  and after 0.015 m of slip, is presented in Figure 6b. At this stage, most of the fault surface is covered by fault gouge. The gouge is made of submicrometer in size clusters of “amorphous-like” particles. Locally, clusters are arranged to form microridges oriented parallel to the slip direction. When  $f = f_p$ , most of the fault surface is covered by amorphous-like material, often arranged in ropy-like structures (Figure 6c). The thickness of the glass-like patches is relatively continuous, and their thickness ranges between 1 and 10  $\mu\text{m}$ . When  $f = f_{ss}$  and after 1.5 m of displacement, the slipping zone is made of a continuous 200  $\mu\text{m}$  thick glass layer (Figure 6d). The fraction of clasts in the glass layer is about 0.22.

### 4.2. In-Fault and Off-Fault Damage Due to Seismic Slip

Four postmortem samples resulting from experiments conducted at 0.003, 0.03, 0.3, and 3 m/s of sliding velocity were investigated to study off-fault crack damage. All four experiments were conducted at the same effective normal stress ( $\sigma_n^{\text{eff}} = 20$  MPa) and similar final slip ( $\approx 3$  m). Thin sections were made perpendicular to the fault surface and to the sliding direction.

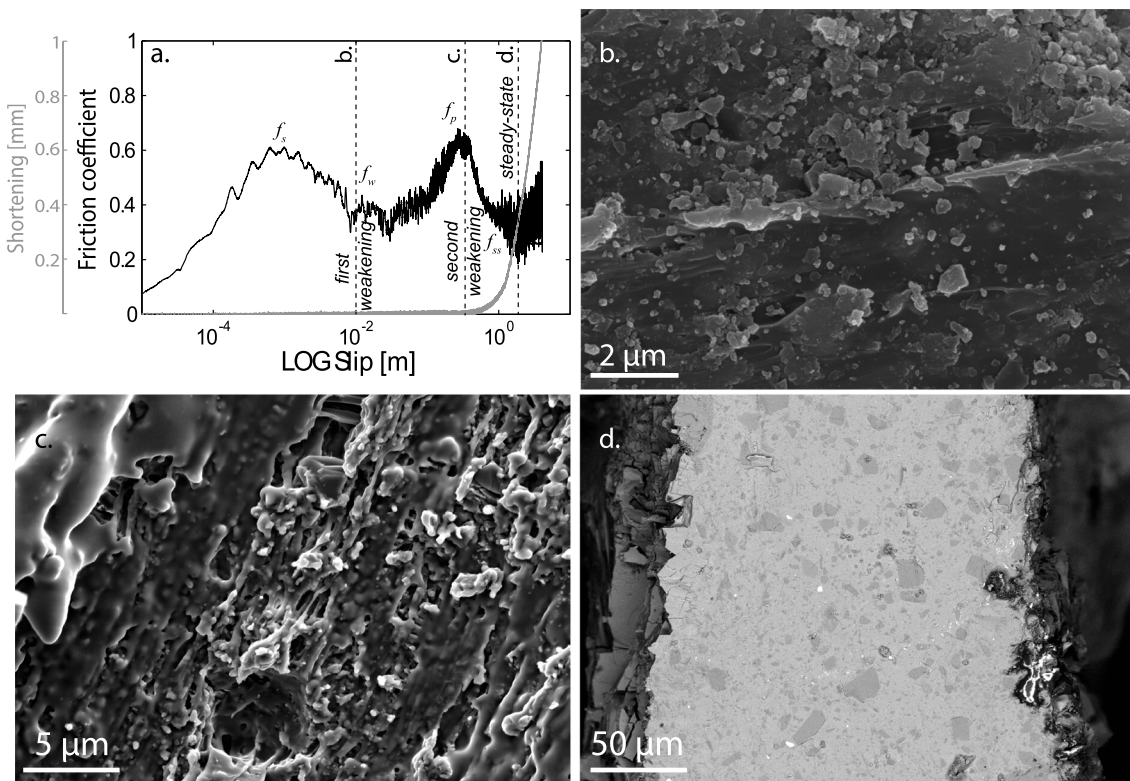


**Figure 6.** Evolution of the fault surface and the slipping zone with increasing slip. (a) Experiments were stopped at the completion of first weakening, strengthening, and during steady state. (b) Slipping zone after 0.015 m of slip. The fault surface is decorated by aggregates of subrounded submicrometer in size particles. Locally, aggregates appear to be aligned to form slickenlines. However, most of the fault surface remains devoid of glass. (c) Fault surface after 0.5 m of slip (initiation of the second weakening). At this step, large but discontinuous glass patches cover the sliding surface. (d) Cross section of the slipping zone after 1.5 m of slip (steady state conditions). A continuous glass layer of 200 μm in thickness separates the wall rocks. The fraction of clasts into the melt layer is about 0.22 (i.e., 22%).

At low sliding velocity ( $V_s = 0.003$  m/s), intense fracturing is observed in the first 0.2 mm next to the slipping zone (Figure 7a). In addition, no glass was found on the fault surface.

At 0.03 m/s, grain size reduction is observed in the slipping zone. In addition, some parts of the fault surface are covered with amorphous-like material, similar to the one shown in Figure 6c. Intergranular cracks are more diffuse than in intact Westerly granite samples, up to a distance of 2 mm from the slipping zone (Figure 7b). However, almost no intragranular cracks are observed.

Higher slip rates always lead to the melting of the slipping zone (see glass layer in Figures 6, 7c, and 7d). The thickness of the glass layer increases with the sliding velocity from 100 μm and 300 μm at 0.3 and 3 m/s, respectively, while the fraction of clasts into the glass layer decreases with  $V_s$ .

An important observation is that the wall rocks present substantial off-fault damage and diffuse intragranular and intergranular cracks (Figures 7c and 7d). In particular, the damage in the wall rocks is more pervasive in the samples sheared at 0.3 m/s than in the one sheared at 3 m/s. More cracks are observed at a given distance to the fault plane during experiments conducted at 0.3 and 0.03 m/s (Figure 7c). The microstructural results are in agreement with our elastic wave velocities measurements on postmortem samples, which are indicative of larger off-fault damage in the samples sheared at 0.3 m/s (Figure 5). Finally, in all samples studied, we observe at least quantitatively a continuous decrease of the amount of cracks as a function of the distance from the fault surface. These results are in agreement with previous studies [Tanikawa et al., 2010].

## 5. Discussion

### 5.1. First Weakening Stage: Flash Heating

The relationships between effective normal stress, sliding velocity, power density ( $\tau V_s$ ), and the characteristics of the first weakening stage are presented in Figure 8. The peak friction of the experimental fault ( $f_s$ ) is

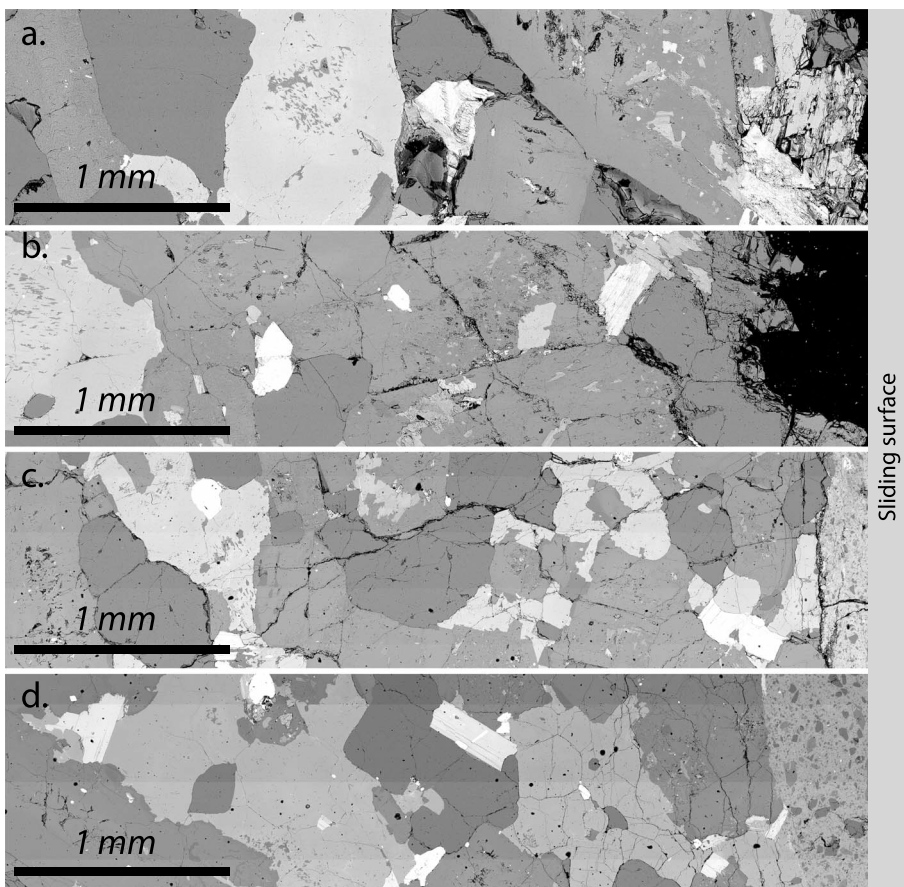


**Figure 7.** Microfracturation in the wall rocks induced during high-velocity experiments. Micrographs of thin sections of the slipping zones of experiments (a) s657, (b) s663, (c) s664, and (d) s675, conducted, respectively, at 0.003 m/s, 0.03 m/s, 0.3 m/s, and 3 m/s. All these experiments were performed under 20 MPa effective normal stress and under room humidity conditions.

observed when the sliding velocity is close to a critical value  $V_c$ , which corresponds to the slip velocity required to initiate the first weakening stage. Values of  $V_c$  range from 0.075 to 0.13 m/s (Figure 8a). The effective normal stress acting on the fault has no influence on  $f_s$  (Figure 8b), and values of the friction coefficient are generally close to 0.7, in agreement with Byerlee [1978]. Once  $V_s$  becomes greater than  $V_c$ , the first weakening initiates and the friction coefficient decreases up to  $f_w$ . If the target value of  $V_s$  remains below  $V_c$  during the entire experiment, this first weakening stage is not observed, similarly as in experiments conducted at 0.003, 0.01, and 0.03 m/s (Tables 1 and 2). Note that this weakening stage is not observed during water-saturated experiments.

The magnitude of  $f_w$  mainly depends on  $V_w$  (i.e., the peak of velocity during experiments at  $f = f_w$ ) (Figure 8a). The larger the sliding velocity  $V_w$  during this stage, the larger the weakening of the fault (i.e., the lower  $f_w$ ). The effective normal stress and the power density dissipated in the slipping zone do not affect this weakening state (Figures 8b and 8c).

The first weakening observed during experiments at high slip rate ( $V_s > V_w$ ) only depends on the sliding velocity (Figure 8). This weakening occurs for small displacement ( $\approx 1$  cm) and during the acceleration part of the experiments. During this weakening, AE intensity continuously decreases with the friction coefficient, and no AE activity is observed when  $f = f_w$  (Figure 3c). The effective normal stress acting on the fault does not affect the intensity of the weakening (Figure 8b), suggesting that the activation of this weakening is induced at the scale of asperities where the local stress is much larger than the macroscopic stress. These results can be interpreted using flash heating theory [Rice, 2006]. During the acceleration part of the experiments,  $f$  first increases

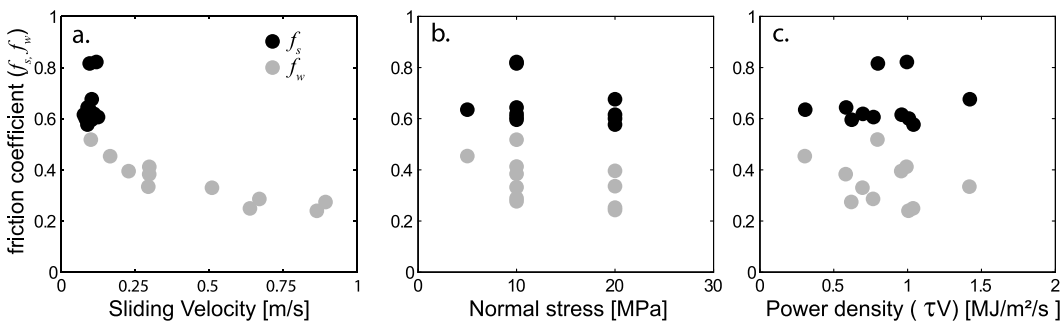


**Figure 8.** First weakening stage. (a) Initial quasi-static friction coefficient ( $f_s$ ) and at the end of the first weakening stage ( $f_w$ ) with increasing sliding velocity. (b)  $f_s$  and  $f_w$  for increasing effective normal stress. (c)  $f_s$  and  $f_w$  for increasing frictional power density dissipated in the slipping zone.

at values comparable to the static friction coefficient ( $f_s \approx 0.6$ ). When  $V_s$  reaches a critical sliding velocity ( $V_c$ ),  $f$  decreases down to  $f_w$ . Using our experimental data, the critical weakening velocity can be estimated around 0.1 m/s.

This critical sliding velocity can be predicted by the flash heating theory following [Rice, 2006]

$$V_c = \frac{(\rho C_h)^2 (T_w - T_i)^2 \pi \kappa}{(\tau_c)^2 a} \quad (3)$$

where  $\rho$  is the rock density,  $C_h$  is the heat capacity,  $T_w$  is the melting temperature of Westerly granite,  $T_i$  is the initial rock temperature,  $\kappa$  is the heat diffusivity,  $\tau_c$  is the contact shear strength of asperities, and  $a$  is the average size of asperities ( $a = 10 \mu\text{m}$ ). The contact shear strength of asperities  $\tau_c$  was set as the average hardness  $H_{\text{ave}}$  of minerals composing Westerly granite times a static friction coefficient ( $f_s$ ) of 0.6 [Byerlee, 1978] ( $\tau_c = H_{\text{ave}} f_s = 5.6 \text{ GPa}$ ). Estimation of  $V_c$  following equation (3) using thermal parameters for westerly granite [Goldsby and Tullis, 2011; Passelègue et al., 2014a] is compatible with our measurements of  $V_c$  at  $f = f_s$  (Figure 9) ( $V_c \approx 0.1 \text{ m/s}$ ). In addition, the evolution of  $f$  as a function of  $V_s$  and  $V_w$  when  $V_s > V_w$  can be predicted by [Rice, 2006]

$$f = (f_s - f_{ss}) \frac{V_c}{V_s} + f_{ss} \quad (4)$$

where  $f_s$  and  $f_{ss}$  are, respectively, the average values of the static and steady state friction coefficients. The trend described by experimental results is in good agreement with flash heating theory (Figure 9), suggesting that the first weakening is due to the melting of asperities, as suggested by the presence of amorphous-like, probably glassy, clusters of nanoparticles covering the fault surface (Figure 6b). In the presence of water, this first weakening is not observed in the range of velocity tested. This result can be explained by the presence of water which reduces the rise of temperature at the asperity contact, inducing an increase of the critical velocity allowing flash heating phenomena, as highlighted in a previous study [Violay et al., 2014].

## 5.2. Second Weakening Stage: Melt Lubrication

Figure 10 presents the influence of the effective normal stress  $\sigma_n^{\text{eff}}$ , the sliding velocity  $V_s$ , and the power density on  $f_p$ ,  $f_{ss}$ , and  $D_{ss}$ . The second weakening stage is followed by a strengthening stage after a few decimeters of slip (Figure 2). This second peak of strength of the fault  $f_p$  decreases with increasing sliding velocity;  $f_p$  is about 0.8 at low sliding velocity ( $V_s < 0.1 \text{ m/s}$ ) and decreases down to 0.6 at higher sliding velocity ( $V_s > 1 \text{ m/s}$ ) (Figure 10a). While the effective normal stress does not seem to have a strong influence on  $f_p$  independently of  $V_s$  (Figure 10b), the increase of the power density ( $\tau V_s$ ) induces the exponential decrease of  $f_p$  (Figure 10c). These results suggest that the strengthening observed during the transition between the two slip-weakening stages is a function of the energy dissipated along the fault. This strengthening is due to transient thermal behavior of the slipping zone during the initial stages of bulk melting [Hirose and Shimamoto, 2005]. The first large melt patches are highly viscous because of the low temperature and the abundance of clasts, inducing a fault strengthening.

Once the strength of the fault reaches  $f_p$ , an exponential decay is observed until the friction reaches its steady state value ( $f_{ss}$ ) (Figure 2). This second weakening stage has been widely observed in previous studies [Tsutsumi and Shimamoto, 1997; Hirose and Shimamoto, 2005; Di Toro et al., 2006; Niemeijer et al., 2011]. The second weakening is a function of sliding velocity and frictional power density dissipated in the slipping

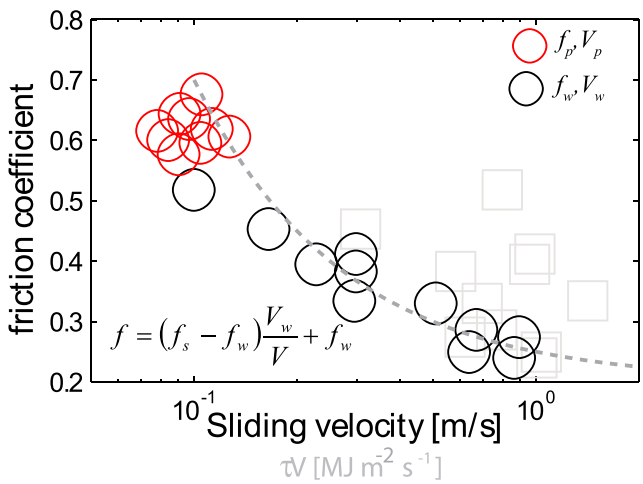


**Figure 9.** Comparison between the first measured weakening and weakening inferred by flash heating theory (grey dashed line) [Rice, 2006]. Red circles correspond to values of the friction coefficient at the first peak of strength ( $f_p$ ). Black circles correspond to values of  $f_w$  as a function of  $V_w$ . Grey empty squares present the same data set of the black circles (i.e.,  $f_w$ ) but as a function of the frictional power density  $\tau V_w$ .

zone (Figures 10a and 10c), in agreement with previous studies [Hirose and Shimamoto, 2005; Nielsen et al., 2008; Di Toro et al., 2011].

The data reported in Figure 10 suggest that the production of the frictional heat along the fault surface mainly controls the intensity of the weakening. The decrease of the friction coefficient is explained by the increase of the melt temperature which decreases its viscosity and so the strength of the fault. Even under low effective normal stress conditions,  $f_{ss}$  can reach low values if the sliding velocity is high enough compared to the heat diffusion and if the final displacement is larger than  $D_{ss}$ .

Both  $f_{ss}$  and  $D_{ss}$  decrease as a power law with increasing power density (Figures 10c and 10f). The steady state friction coefficient  $f_{ss}$  decreases following  $f_{ss} \propto 0.34(\tau V_s)^{-1/6}$  and  $D_{ss}$  following  $D_{ss} \propto 1.6(\tau V_s)^{-1/4}$ .

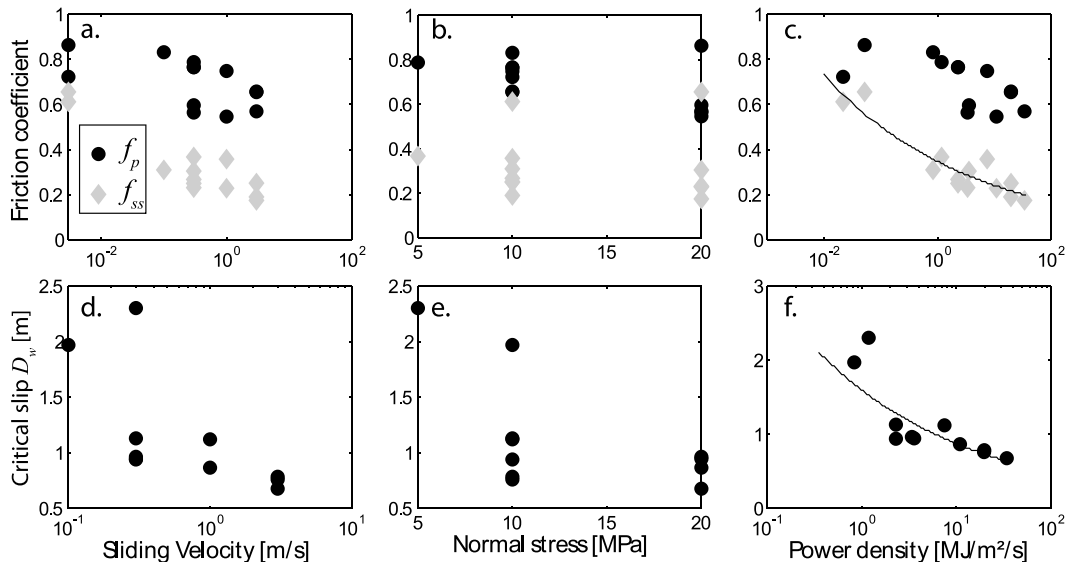


**Figure 10.** Influence of effective normal stress, sliding velocity, and frictional power density on the second weakening stage. (a) Friction coefficient ( $f_p$ ) and during steady state ( $f_{ss}$ ) with increasing sliding velocity. (b) The  $f_p$  and  $f_{ss}$  for increasing effective normal stress. (c) The  $f_p$  and  $f_{ss}$  for increasing frictional power density dissipated in the slipping zone. Black solid line corresponds to the best fit  $f_{ss} \propto 0.34(\tau V_s)^{-1/6}$ . (d) Slip-weakening distance ( $D_{ss}$ ) with increasing sliding velocity. (e)  $D_{ss}$  for increasing effective normal stress. (f)  $D_{ss}$  for increasing frictional power density dissipated in the slipping zone. Black solid line corresponds to the best fit  $D_{ss} \propto 1.6(\tau V_s)^{-1/4}$ .

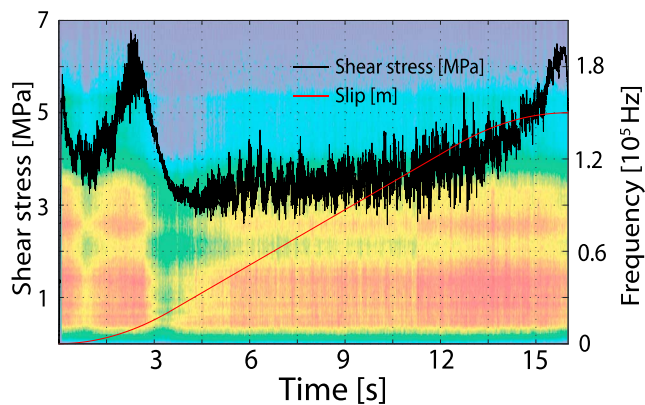


**Figure 11.** Power spectrum of a complete acoustic waveform during experiment s662 conducted at  $V_s = 0.3$  m/s and  $\sigma_n^{\text{eff}} = 10$  MPa and room humidity conditions.

These results are in agreement with previous studies on silicate-bearing rocks [Hirose and Shimamoto, 2005; Niemeijer et al., 2011]. Another observation here is that the initiation of large sample shortening occurs when  $D$  reaches  $D_{ss}$ , which suggests that large shortening also decreases following a power law with power density, and is related to the heat production along the fault.

### 5.3. Decrease of the AE Activity Due to Thermal Degradation of the Fault Surface

#### 5.3.1. Low Sliding Velocity Experiments

At low sliding velocity ( $V_s = 0.003$  m/s), a small weakening is observed as a function of the displacement. Acoustic emissions in this case are probably due to wear and grain size reduction in the slipping zone. Bursts of AEs are generally associated with the decrease of the friction coefficient, suggesting that the decrease of the friction coefficient is due to the failure of asperities in the slipping zone. Asperity and grains failure releases the stress accumulated in the slipping zone. Another possible source of AEs can be the propagation of cracks approaching the free surface of the rock assemblage, inducing tensile stress at the boundaries.

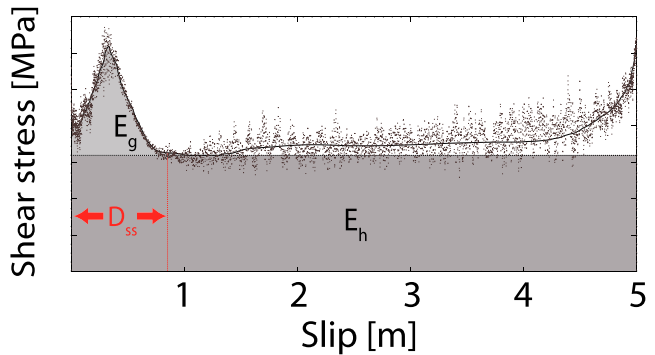
#### 5.3.2. High Sliding Velocity Experiments

Figure 11 presents the correlation between the frictional behavior of the slipping zone and a spectrogram of the complete acoustic waveforms recorded during an experiment conducted at  $V_s = 0.3$  m/s and  $\sigma_n^{\text{eff}} = 10$  MPa. As explained before, the first weakening is due to the melting of asperities, as suggested by postmortem sample analysis (Figure 6b) and by the comparison between experimental data and flash heating theory [Violay et al., 2014]. Flash heating of asperities may explain the decrease of AE activity during this first weakening. Indeed, sliding velocities high enough to trigger flash heating lead to a sudden temperature increase of the contact asperities during their lifetime, so that asperities deform plastically rather than in a brittle manner [Rice, 2006; Rempel and Weaver, 2008; Beeler et al., 2008]. Melting of asperities inhibits brittle failure mechanisms and the occurrence of AE in the slipping zone (Figure 11).

During the subsequent strengthening, an increase of the AE activity is observed. During this stage, asperities vanish as melt patches grow along the fault surface. However, parts of the fault may remain unlubricated, leading to abrasive and adhesive wear [Spray, 1995] which may explain the increase in AE release rate. However, once the shear stress reaches the second peak of strength, a continuous molten layer is formed, which may explain the second decrease of the AE activity at the onset of melting (Figure 11). The formation of a continuous layer of melt in the slipping zone leading to  $f_{ss}$  is confirmed by movies of similar experiments recorded with a high-speed infrared camera [Niemeijer et al., 2011]. The AE activity vanishes until the friction coefficient reaches its steady state value (Figure 11). Because AEs are due to the propagation of cracks and cracks require fracture energy to propagate, we discuss below the occurrence of AEs during experiments with direct measurements of fracture energy  $E_g$  deduced from the shear stress versus displacement curves.

### 5.4. Fracture Energy Inferred From High-Velocity Friction Experiments

A widely used parameter to quantify damage during seismic slip is the “effective” fracture energy ( $E_g$ ). Figure 12 presents a simplified scheme of the energy budget in high-velocity friction experiments. The scheme mimics those proposed for natural earthquakes.



**Figure 12.** Energy budget during high-velocity friction experiments. The scheme mimics those proposed for natural earthquakes [Kanamori and Rivera, 2006], and  $E_g$  corresponds to the fracture energy. We only consider the fracture energy during the friction drop.  $E_h$  corresponds to the frictional energy generally assumed to be dissipated into heat. However, field and experimental data suggest that most of  $E_g$  is also heat [Pittarello et al., 2008; Di Toro et al., 2012; Passelègue et al., 2016]

In these experiments, there is no rupture front and the radiated energy cannot be estimated. However, both  $E_g$  and  $E_h$  can be estimated directly using experimental curves as shown in Figure 12. We calculated the evolution of  $E_g$  as a function of the displacement following

$$E_g = \int_0^{D_{ss}} (\tau_{(\Delta D)} - \tau_{ss}) dD \quad (5)$$

where  $D$  is the displacement at a given time, and  $\tau_{ss}$  is the steady state shear stress.  $E_g$  was calculated for all experiments.

An abrupt increase of  $E_g$  is generally observed up to the steady state friction. However, when  $D_{ss}$  is reached, the fracture energy reaches a maximal value during HVF experiments on crustal rocks [Nielsen et al., 2016], even if small variations can be observed due to the initiation of the shortening.

We compared the evolution of the fracture energy with the occurrence of AEs during HVF experiments conducted at 0.3 and 3 m/s under two different effective normal stress conditions (respectively,  $\sigma_n^{\text{eff}} = 10$  and 20 MPa) (Figure 13). As stated previously, most of the increase of fracture energy  $E_g$  dissipated in the slipping zone is observed when  $D < D_{ss}$ . However, few AEs are recorded for  $D < D_{ss}$ . Most of the AE are recorded for  $D > D_{ss}$ , when the friction coefficient is equal to  $f_{ss}$ . In addition, more AEs are observed at 0.3 m/s than at 3 m/s, in agreement with our microstructural observations and our measurements of elastic wave velocities which suggest larger off-fault damage at 0.3 m/s (Figure 5). The effective normal stress also presents an influence on the amount of AEs recorded. In the case of experiments conducted at 0.3 m/s, more AEs are recorded at 20 MPa than at 10 MPa effective normal stress. This is not the case at 3 m/s sliding velocity because in this case, the shear stress acting on the fault is comparable at 10 and 20 MPa effective normal stress, due to larger weakening at 20 MPa. This result suggests that the shear stress has much more influence on AE activity than the effective normal stress acting on the fault. Finally, the amount of slip also controls the amount of AEs. At given conditions, the larger the slip, the larger the number of AEs recorded. The main observation here is that the initiation of large shortening occurs after  $D_{ss}$ , suggesting that few cracks propagate for  $D < D_{ss}$  into the rock samples, in agreement with the lack of AEs.

The production of AEs when  $D > D_{ss}$  may be explained by heat diffusion within the rock sample. Indeed, AEs could be linked to thermal cracking, as the heat diffuses away from the slipping zone. This hypothesis is supported by (i) our analysis of the microfracturing which highlighted the presence of cracks at a distance from the slipping zone at high slip rates (Figure 7), (ii) the decrease in cracks density from the slipping zone to the wall rock, (iii) the fact that AEs are still recorded after the end of the experiments (Figure 3c), and (iv) that few AEs have been recorded during water-saturated experiments (Figure 4c).

### 5.5. Heat Diffusion, Thermal Cracking, and AE

#### 5.5.1. Heat Production During HVF

Thermal cracking is dependent upon the temperature, thermal expansion mismatch between the minerals composing the granite, thermal expansion anisotropy of individual minerals, initial crack porosity, and the

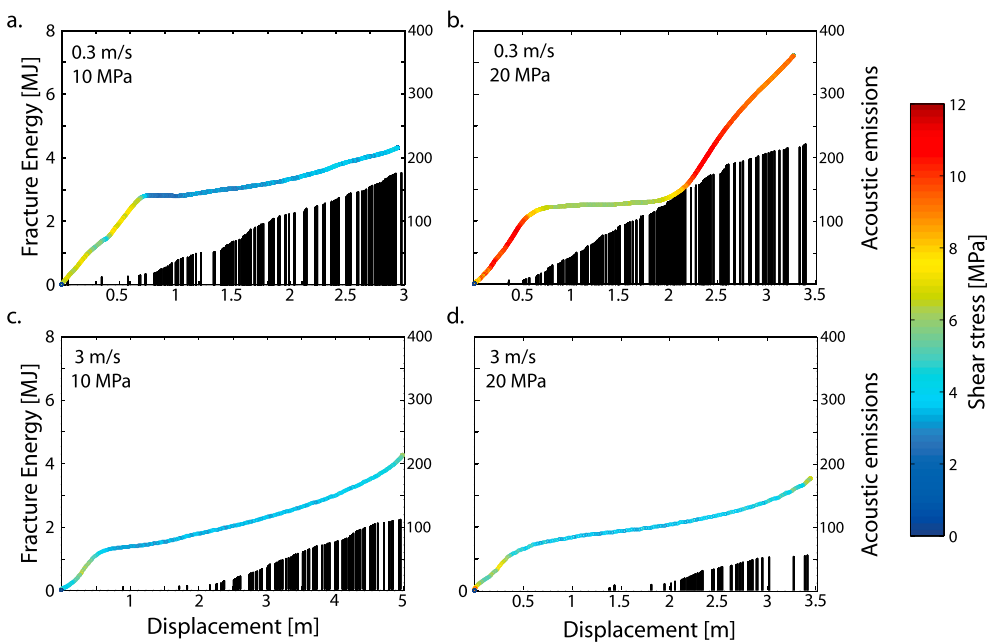


**Figure 13.** Influence of sliding velocity and effective normal stress on AE activity. Experiments (a) s662, (b) s664, (c) s666, and (d) s675. Black solid bar corresponds to the cumulative number of AEs. The colorbar presents the evolution of the shear stress acting along the fault during experiments.

average grain size. To quantify the increase in temperature and the diffusion of the heat within the rock sample, we integrated numerically the energy converted into heat using a simple one-dimensional finite difference model. The sample is considered as homogeneous and isotropic and no heat loss by radiation is assumed, leading to an upper bound of the final temperature. We assume that all the mechanical energy is converted into heat, and we estimated the heat flux following

$$Q(t) = 0.5\tau(t)V_e \quad (6)$$

where  $V_e$  is the equivalent sliding velocity in the central part of the fault and  $\tau(t)$  is the shear stress history described using the following empirical law [Hirose and Shimamoto, 2005]

$$\tau(t) = \tau_0 \exp\left(\frac{\ln(0.05)V_e t}{D_{ss}}\right) + \tau_{ss} \quad (7)$$

where  $\tau_0$  is the peak of shear stress defined by  $\tau_0 = \sigma_n^{\text{eff}} * f_s$  and  $\tau_{ss} = \sigma_n^{\text{eff}} * f_{ss}$  corresponds to the steady state shear stress. In the numerical simulations,  $D_{ss}$  and  $f_{ss}$  are calculated as a function of the power density using the empirical fit described above,  $f_{ss} \propto 0.34(\tau V_s)^{-1/6}$  and  $D_{ss} \propto 1.6(\tau V_s)^{-1/4}$ . During the slip history, we assume a single exponential decay of the stress as proposed by [Hirose and Shimamoto, 2005] (see equation (7)). The latter assumption is robust in terms of energy because the integration of both experimental and empirical shear stress curves versus slip leads to similar values of energy input into the specimen (Figure 14). Thus, the heat equation is written as follows [Carslaw and Jaeger, 1959]:

$$\frac{\partial T}{\partial t} = \frac{Q(t)}{h\rho C_h} + \kappa \frac{\partial^2 T}{\partial x^2} \quad (8)$$

where  $h$  is the width of the heat production zone (here  $h = b$ , with  $b$  the average grain size of the Westerly granite  $\approx 0.25$  mm [Fredrich and Wong, 1986]). Equation (8) is integrated numerically using the parameters presented in Table 3, and the heat diffusion is implicitly calculated as a function of the temperature following

$$T^{n+1} = \kappa \left[ 2 \frac{T_{i+1}^{n+1} - T_i^{n+1}}{\Delta x_i(\Delta x_i + \Delta x_{i+1})} - 2 \frac{T_i^{n+1} - T_{i-1}^{n+1}}{\Delta x_i(\Delta x_i + \Delta x_{i-1})} \right] \quad (9)$$

where  $n$  is the time step and  $i$  refers to the location in the finite difference grid. Each element of the grid has a size of 0.5 which roughly corresponds to the average size of the grains. Because the temperature of the fault

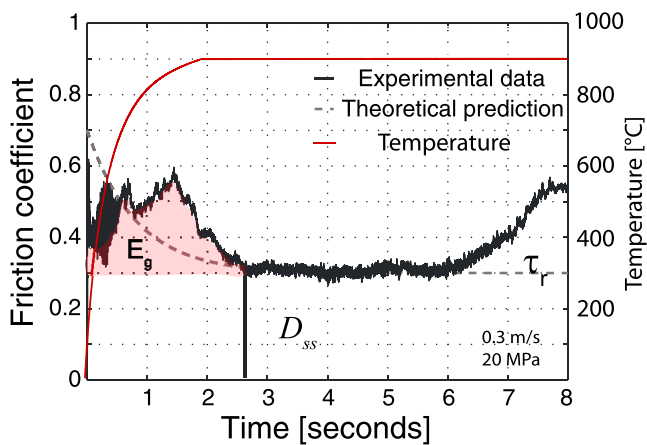


**Figure 14.** Comparison between experimental decay of the friction during experiment s664 conducted at 0.3 m/s under 20 MPa effective normal stress and the theoretical prediction using equation (7). While the shape of the curve is different due to the lack of the first weakening in the theoretical curve, the energy input in the system is similar. The red line corresponds to the theoretical estimation of the temperature rise during the experiments. The estimation is in agreement with the formation of a continuous layer of melt in the slipping zone (Figure 6c).

surface cannot exceed the melting temperature of the granite, once  $T(n) = T_w$ , the fault surface temperature is kept constant and we just consider the diffusion of heat. Despite the differences in the first weakening stage, the modeled temperature is consistent with experimental results showing that the bulk melting temperature is reached during the second weakening, as confirmed by the presence of a continuous melt layer of glass along the slipping zone (Figure 6c).

Figure 15a presents the temperature profiles into the rock specimens for simulations at 0.3 and 3 m/s and for, respectively, 5, 10, and 20 MPa effective normal stress. All simulations have been performed for an equivalent final displacement ( $D_f = 3$  m). The main result is that the heat is better diffused into the rock specimen at 0.3 m/s than at 3 m/s, because the sliding time is longer (10 s versus 1 s) (Figure 15a). The effective normal stress has little influence on average heat diffusion length scale, as observed in our experiments.

### 5.5.2. Theoretical Approach of Thermal Cracking

Using the thermal model described above, we now quantify damage induced by thermal cracking in the rock specimen. Following *Fredrich and Wong* [1986], we assume that the thermoelastic strain energy results in strain mismatches and incompatibilities that are dissipated into surface energy by microcrack propagation. Here we simply consider that the total fracture energy generated by thermal cracking corresponds to an increase of crack surface area ( $S_v - S_{v0}$ , where  $S_{v0}$  is the initial surface of all the cracks), multiplied by the average specific surface energy of minerals for mode I crack propagation ( $\gamma_c^1$ ). In such case, the energetic balance is written [*Fredrich and Wong*, 1986] as

$$Eg_{th} = (S_v - S_{v0})\gamma_c^1 = 0.125 \frac{E}{1-\nu} (\Delta\alpha)^2 (T - T_i)^2 \quad (10)$$

**Table 3.** Parameters Used for Heat Diffusion and Thermal Cracking Estimation<sup>a</sup>

Parameter	Symbol	Value	Unity
Rock density	$\rho$	2650	$\text{kg m}^{-3}$
Young Modulus	$E$	46	GPa
Poisson ratio	$\nu$	0.1	-
Heat capacity	$C_h$	900	$\text{J kg K}^{-1}$
Weakening temperature	$T_w$	900	°C
Room temperature	$T_i$	25	°C
Thermal diffusivity	$\kappa$	$1.25 \times 10^{-6}$	$\text{m}^{-2} \text{s}^{-1}$
Grain size	$b$	0.00025	m
Specific surface energy	$\gamma_c^1$	7.5	$\text{J m}^{-2}$
Thermal expansion mismatch	$\Delta\alpha$	$5.5 \cdot 10^{-6}$	MPa

<sup>a</sup>Physical parameters from *Wong* [1982] and *Fredrich and Wong* [1986].

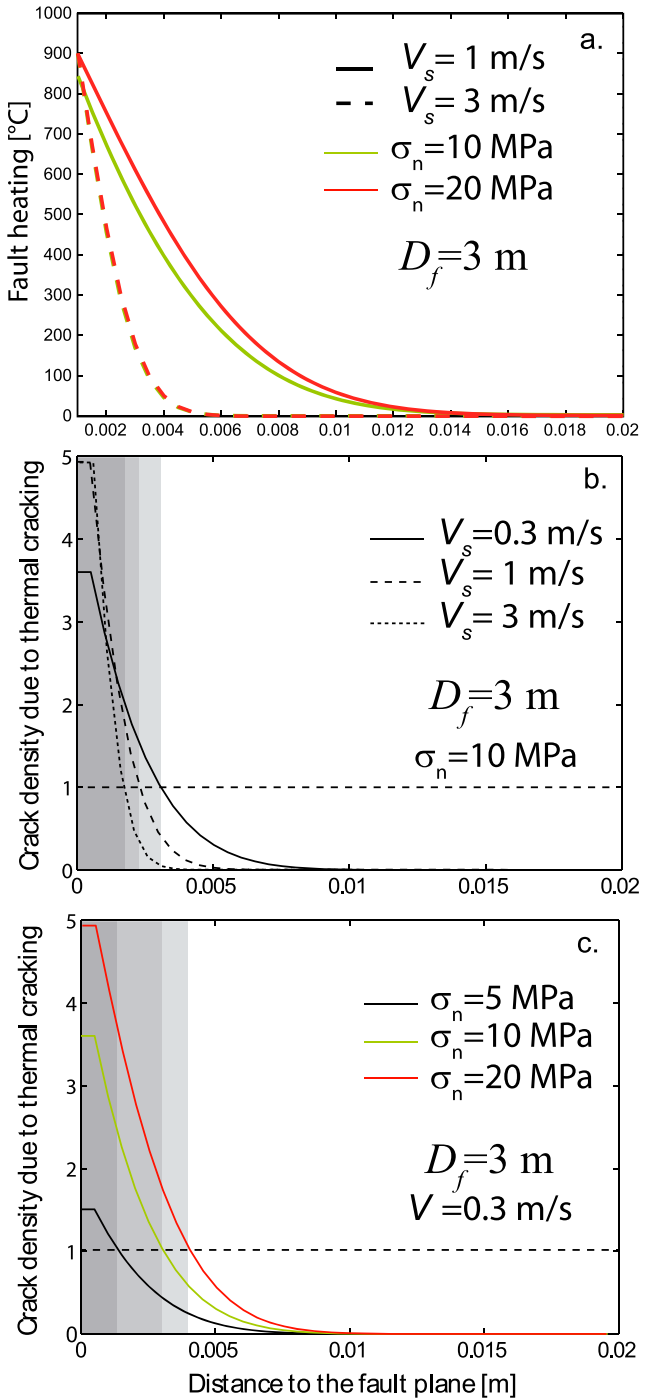


**Figure 15.** Temperature evolution and consequent off-fault damage during high-velocity friction experiments. Simulations were conducted for two pressure conditions (respectively,  $\sigma_n^{\text{eff}} = 10$  and 20 MPa) and for three sliding velocities (respectively, 0.3, 1, and 3 m/s). (a) Temperature profiles within the rock specimens after 3 m of slip. Influence of (b) sliding velocity and (c) effective normal stress on thermal cracking. The grey areas represented in Figures 15b and 15c correspond to the thickness of the sample for which  $\rho_{th} > 1$ , i.e., a good proxy for the final shortening of the sample.

where  $Eg_{th}$  is the thermal fracture energy,  $E$  is the Young's modulus of the granite,  $\gamma_c^1$  is the average specific Griffith surface fracture energy for minerals, and  $\Delta\alpha$  is the isotropic thermal expansion mismatch defined by  $\alpha = \alpha_{ii}^1/3 - \alpha^0$ , with  $\alpha^0$  the thermal expansion of the matrix. While the estimates of the temperature increase have upper bound values (melting point), this is not the case for the estimates of the final value of the thermal cracking energy because (i) we are not taking into account the sample shortening, which involves that the heat source actually also "diffuses" into the sample; (ii) we are assuming that within each grid point, the temperature profile is linear, thus neglecting the effects of thermal shocking, i.e., potential microcracking due to the nonlinearity of the temperature gradient; and (iii) we are not taking account of the  $\alpha/\beta$  transition in quartz [Glover et al., 1995]. The contribution of the latter may become important in the immediate vicinity of the slipping zone, but its determination is beyond the scope of this study.

Estimating the thermal fracture energy using (10) for experiments leads to values in the order of  $100 \text{ kJ/m}^2$ .  $E_g^{\text{th}}$  remains close to but smaller than the energy required to produce the same amount of shortening by melting, using a latent heat of  $220 \text{ kJ/kg}$  for granite. Following these results, thermal cracking process is more efficient than melting process in granite and is supposed to be the dominant process explaining the shortening during experiments. According to this, the melt extrusion rate approximates the shortening rate due to thermal cracking. The wall rocks are cracked and then melted, as suggested by Spray [1995].

This thermal fracture energy is effectively an important process in the shortening because it is converted into newly formed cracks in the rock specimen during faulting. Using equation (10), we can approximate quite reasonably the crack density  $\rho_{\text{th}}$  due to thermal cracking during experiments following [Fredrich and Wong, 1986; Wang et al., 2013]

$$\rho_{\text{th}} = 0.125 \frac{b}{\gamma_c^1} \frac{E}{1-\nu} (\Delta\alpha)^2 (T - T_i)^2 \quad (11)$$

where  $b$  is the average grains size. The inferred crack density corresponds to the volume of thermally induced cracks affecting the grains of the intact rock. In the present case (Westerly granite), we mainly considered microline grain boundary and quartz inclusion intergranular cracking [Fredrich and Wong, 1986]. Because shortening initiates when grains and rocks loose cohesion, this estimation of thermal crack density at the scale of the grains is representative to describe wear and shortening processes.

Combining equation (11) with the heat diffusion simulation, we predict that the thermal crack density decreases with distance to the fault plane (Figures 15b and 15c), in agreement with our SEM images of wall rocks (Figure 7). Figure 15b presents the results of simulations for sliding velocities of, respectively, 0.3, 1, and 3 m/s under 10 MPa of effective normal stress. Note that  $\rho_{\text{th}} = 1$  is a maximum physical value, beyond which fragmentation occurs [Guegen and Palciauskas, 1995]. Beyond this upper bound for crack density, thermal fracture energy may be further dissipated by grain size reduction and comminution, potentially leading to a complete mechanical amorphization [Pec et al., 2012]. An additional limitation might also occur when the melting temperature  $T_w$  is reached, because the temperature is bounded by  $T_w$  in the model. In the simulations,  $T_w$  is reached for  $V_s = 3$  and 1 m/s only (Figure 15b).

Nevertheless, the model suggests a substantial "diffusion" of the crack density front away from the fault plane, as  $\rho_{\text{th}}$  increases close to the fault plane. Because it is driven by heat diffusion, thermal cracking is largest in the intermediate sliding velocity range. For example,  $\rho_{\text{th}} = 0$  at 4 mm to the fault plane when  $V_s = 3$  and 1 m/s, while  $\rho_{\text{th}} = 0.35$  for the simulation corresponding to a sliding velocity of 0.3 m/s (Figure 15b).

Secondly, we modeled the influence of the effective normal stress on the crack density for experiments conducted at the same slip velocity (here 0.3 m/s) (Figure 15c). Increasing  $\sigma_n^{\text{eff}}$  leads to the increase of the crack density close to the fault plane up to  $D = D_{ss}$ . In addition, by increasing the effective normal stress, the power density increases as more heat is produced and diffuses into the rock specimen. These two observations combined suggest that the production of thermal cracks is a function of both the power density and of the heat diffusion within the rock sample.

### 5.5.3. Consequences of Thermal Cracking Processes on Shortening Rate

As stated previously, when  $\rho_{\text{th}}$  becomes greater than 1, we may assume that cohesion is lost and fragmentation is reached. Defining the thickness where  $\rho_{\text{th}} = 1$  (Figures 15b and 15c) as a critical value above which shortening of the rock sample may take place, the numerical results reveal themselves as good proxy to estimate the final shortening of the rock sample during high-velocity friction experiments (Figure 16 and Table 1).

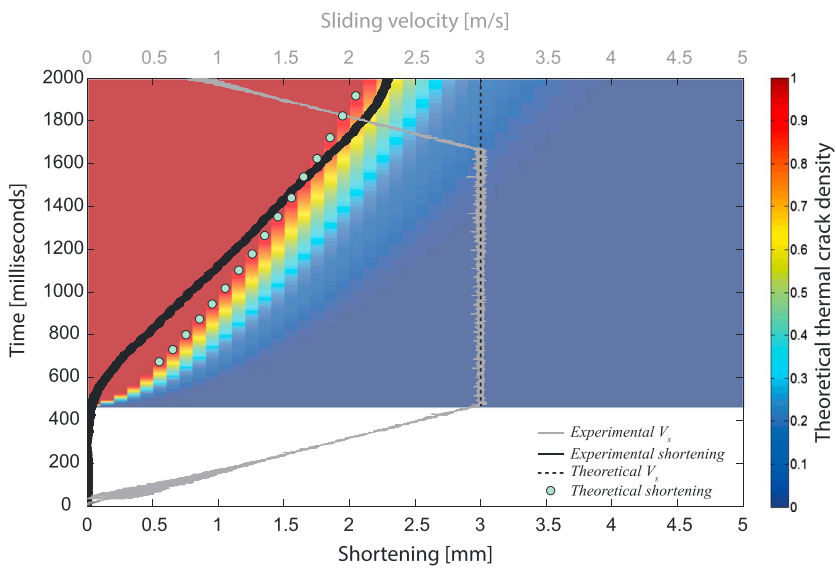


**Figure 16.** Comparison between the experimental shortening and the shortening front inferred from thermal cracking mechanism. Experimental data from experiment s666 conducted at 10 MPa effective normal stress and 3 m/s sliding velocity. The color map presents the modeled advance of the shortening front assuming that shortening of the rock initiates when the thermal crack density becomes greater than 1. The modeled shortening front is highlighted by the green circles. Black solid line corresponds to the experimental shortening. Grey line corresponds to the sliding velocity history during the experiment. The simulation is computed assuming a constant sliding velocity (black dashed line).

Equation (11) can be used to estimate the thermally induced crack density at different distances to the fault plane as a function of the time. We neglect here possible effects due to temperature variation in the radial direction, and we consider that the slip velocity is the same all along the fault (dashed line in Figure 16). Considering that  $\rho_{th} = 1$  highlights the shortening front due to thermal cracking, we can estimate the theoretical shortening due to thermal cracking processes. We reproduced numerically all the experiments conducted under room humidity conditions and compared the experimental values of shortening  $\vartheta$  with the numerical results (Figure 16). Because the sliding velocity is constant in the numerical simulation, both experimental and theoretical shortening rate  $\dot{\vartheta}$  are estimated during the steady state stage of the experiments, observed when

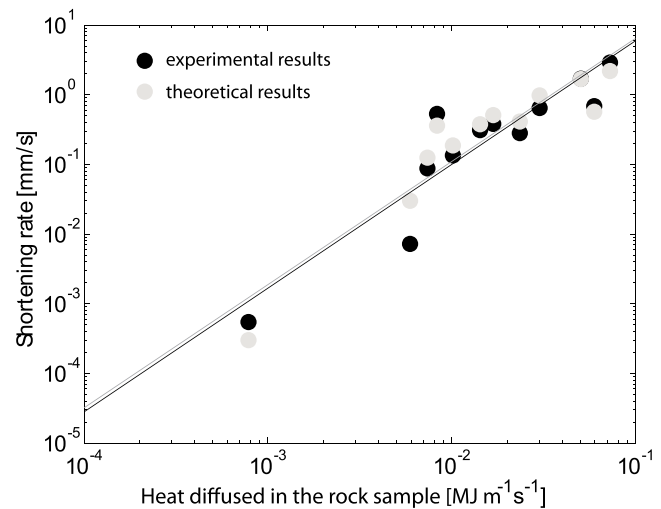


**Figure 17.** Comparison between experimental and theoretical shortening rate as a function of the heat diffused into the rock sample during high-velocity experiments. Black circles correspond to experimental results. Grey circles correspond to theoretical results. The solid lines corresponds to the best fit of each data set.  $\dot{\vartheta}$  evolves as a power law as a function of  $E_\alpha$  following  $\dot{\vartheta} \propto CE_\alpha^{1.8}$ , with  $C \approx 350$ .

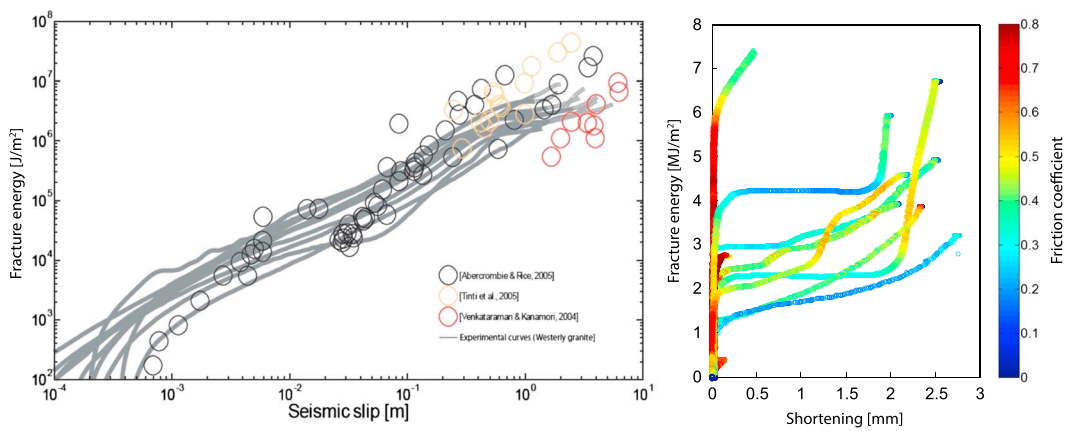


**Figure 18.** Comparison between fracture energy estimated in the experiments and seismological data. All experimental curves present a similar shape, and the final value of  $E_g$  is independent of both  $V_s$  and  $\sigma_n^{\text{eff}}$ . The fracture energy  $E_g$  evolves with displacement as a power law, in agreement with seismological and numerical estimates [Abercrombie and Rice, 2005; McGarr et al., 2004].

the sliding velocity reaches the maximum value and the friction coefficient is at steady state ( $f = f_{ss}$ ) (3 m/s in Figure 16). Theoretical and experimental results are in good agreement.

As stated previously, the production of thermal cracks is a function of both the power density and of the heat diffusion within the rock sample. To further compare experimental and theoretical shortening rate  $\dot{\vartheta}$ , we also compute the average heat diffused  $E_\alpha$  in the rock sample for each experiments following

$$E_\alpha = \tau_0 V_s \sqrt{\pi \kappa \frac{D_f}{V_s}} \quad (12)$$

where  $\tau_0 V_s$  is the power density ( $\text{J m}^{-2} \text{s}^{-1}$ ) and  $\sqrt{\pi \kappa \frac{D_f}{V_s}}$  is an average thermal diffusion length over the course of each experiment. Experimental and theoretical results are presented in Figure 17.

Both experimental and theoretical values of shortening rate  $\dot{\vartheta}$  evolves as a power law as a function of  $E_\alpha$  with  $\dot{\vartheta} = CE_\alpha^{1.8}$ , ( $C \approx 350$ ). These results suggest that the shortening rate is a function of the square of the energy diffused in the rock sample, at least for Westerly granite. Our main conclusion here is that the shortening is not only a function of the heat production but generally occurs when the heat can diffuse in the rock specimen and induce thermal cracking. Another interesting result is that the scaling relation  $\dot{\vartheta} = CE_\alpha^{1.8}$  is also available for experiments presenting low values of power density, i.e., low effective normal stress and slow slip rate. These results suggest that shortening and comminution during seismic slip along faults are related to heat converted into thermal fracture energy, i.e., thermal cracking occurring in fault walls.

## 6. Implication for Natural Earthquakes

The fracture energy term  $E_g$  calculated for each experiment is compared with the seismological estimates of the so-called seismic fracture energy  $G^*$  [Venkataraman and Kanamori, 2004; Abercrombie and Rice, 2005; Tinti et al., 2005, 2009] (Figure 18). In natural earthquakes, the seismic slip scales with the rupture length, i.e., the size of the asperity going to rupture. In our experiments, the fault area is always the same and we just compute the evolution of  $E_g$  as a function of the slip. Our results are, however, comparable to seismological estimates because  $G^*$  also corresponds to an average value normalized by the entire rupture area. Note also that our experiments were mainly conducted under room humidity conditions. While experiments s850 and s851 conducted in the presence of water show similar behavior than room humidity experiments, the results presented here are mainly pertinent to a seismogenic system ideally dry. As observed in a previous study, experimental values of  $E_g$  scale with the final amount of slip [Nielsen et al., 2016]. A notable observation is that  $E_g$  is independent of both  $\sigma_n^{\text{eff}}$  and  $V_s$  (Figure 18) [Nielsen et al., 2016]. Experimental results are in agreement with seismological data calculated using the method described by Abercrombie and Rice [2005] and suggest that  $E_g$  increases as a power law with the seismic slip. Even during experiments conducted at low power densities,  $E_g$  can reach values comparable to natural earthquakes without any evident shortening of the sample (Figure 18).

The main result of this study is that both  $E_g$  and  $E_h$  dissipated during seismic slip contributes to (i) the weakening of faulting [Passelègue et al., 2013, 2016] and (ii) fracturation and grain size comminution within the slipping zone. Our results suggest that field estimates of  $E_g$  [Chester et al., 2005; Ma et al., 2006], which are generally based on grain size reduction in the slipping zone, could be overestimated because a part of the comminution processes occurs after the weakening of the fault and is related to the frictional heat energy  $E_h$ . However, because both  $E_g$  and  $E_h$  are expected to increase with the seismic slip, assuming that the static stress drop is constant in nature (i.e., that the ratio between the slip and the rupture area is independent of the earthquake size), these estimations could be used to infer the total energy dissipated into heat and fracture during natural earthquakes, which corresponds to a part of  $E_g$  and  $E_h$ . Finally, thermal cracking could be reduced by the stress acting at depth. Confinement is also expected to inhibit melt extrusion and to promote lubrication of the fault, reducing the production of heat during seismic slip. However, thermal cracking is supposed to occur during earthquakes along faults at least in the tensional quadrants of faults, where confinement is expected to be locally negligible and where tensional cracks are induced by the rupture tip, allowing the extrusion of melt as suggested by injection veins features [Di Toro et al., 2004].

## 7. Summary

By shearing Westerly granite under room humidity conditions, two drops in friction coefficient are observed. The first drop is independent of effective normal stress and occurs when  $V_s$  becomes greater than a critical value ( $V_c = 0.10 \text{ m/s}$ ) (Figure 8). The second drop occurs after a slip-weakening distance which decreases as a power law with frictional power density ( $\tau V_s$ ) (Figure 10). The first and abrupt drop is explained by flash heating (Figure 9), while the second drop is due to the formation and growth of molten patches in the slipping zone (Figures 6c and 6d). In wet conditions, only the second drop of friction coefficient is observed (Figure 4c). The inhibition of flash heating in the range of velocity tested can be explained by the cooling of asperities due to the presence of water [Violay et al., 2014]. Average values of the fracture energy are independent of effective normal stress and sliding velocity (Figure 18). However, measurements of elastic wave velocities traveling through the fault strongly suggest that higher damage is induced for  $0.1 < V_s < 0.3 \text{ m/s}$  for equivalent final displacement (Figure 5). This observation is also supported by AE recordings. Indeed, most of the AEs are recorded after the initiation of the second drop in friction coefficient, that is, once the slipping zone temperature is high (Figure 13). Some AEs are even recorded a few seconds after the end of the experiments (Figure 3c), suggesting that they may be due to thermal cracking induced by heat diffusion in the rock samples. In addition, the presence of pore fluid pressure (water) delayed the apparition of AEs at equivalent effective pressure, supporting the link between AEs and the production and diffusion of heat (Figure 4c). Using the thermoelastic crack model developed by Fredrich and Wong [1986], we demonstrate that off-fault damage can indeed be induced by heat diffusion. Our theoretical results predict accurately the amount of shortening, supporting the idea that gouge production and gouge comminution is largely controlled by thermal cracking. Once the gouge is formed, part of it is melted and the hot slurry (melt and suspended clasts) extruded from the slipping zone makes the amount of shortening due to thermal cracking similar to the one induced by melting. Finally, we show that thermal cracking during seismic slip, under room humidity conditions, could play a key role both in the evolution of the physical properties of the slip zone and the high-frequency radiation.

## Acknowledgments

We thank Teng-Fong Wong and an anonymous reviewer for insightful comments which greatly improved the manuscript. F.X.P. and A.S. thank Eiichi Fukuyama and Daniel Faulkner for fruitful discussions. This work was supported via the ANR program ANR-12-JS06-0003 "Delf" and via the ERC CoG "NOFEAR" (614705). The data presented in this paper are available by contacting the corresponding author at francois.passelegue@manchester.ac.uk.

## References

- Abercrombie, R. E., and J. R. Rice (2005), Can observations of earthquake scaling constrain slip weakening?, *Geophys. J. Int.*, 162(2), 406–424.  
Abercrombie, R. E., A. McGarr, G. Di Toro, and H. Kanamori (2006), *Earthquakes: Radiated Energy and the Physics of Faulting*, AGU, Washington, D. C.  
Beeler, N. (2006), Inferring earthquake source properties from laboratory observations and the scope of lab contributions to source physics, in *Earthquakes: Radiated Energy and the Physics of Faulting*, *Geophys. Monogr. Ser.*, vol. 170, edited by R. Abercrombie et al., pp. 99–119, AGU, Washington, D. C.  
Beeler, N., T. Tullis, and D. Goldsby (2008), Constitutive relationships and physical basis of fault strength due to flash heating, *J. Geophys. Res.*, 113, B01401, doi:10.1029/2007JB004988.  
Boatwright, J. (1980), A spectral theory for circular seismic sources; simple estimates of source dimension, dynamic stress drop, and radiated seismic energy, *Bull. Seismol. Soc. Am.*, 70(1), 1–27.  
Boullié, A.-M., E.-C. Yeh, S. Boutareaud, S.-R. Song, and C.-H. Tsai (2009), Microscale anatomy of the 1999 Chi-Chi earthquake fault zone, *Geochem. Geophys. Geosyst.*, 10, Q03016, doi:10.1029/2008GC002252.  
Brantut, N., A. Schubnel, J.-N. Rouzaud, F. Brunet, and T. Shimamoto (2008), High-velocity frictional properties of a clay-bearing fault gouge and implications for earthquake mechanics, *J. Geophys. Res.*, 113, B10401, doi:10.1029/2007JB005551.  
Brantut, N., F. X. Passelègue, D. Deldicque, J.-N. Rouzaud, and A. Schubnel (2016), Dynamic weakening and amorphization in serpentinite during laboratory earthquakes, *Geology*, 43, 932–1.  
Brune, J. N., T. L. Henley, and R. F. Roy (1969), Heat flow, stress, and rate of slip along the San Andreas fault, California, *J. Geophys. Res.*, 74(15), 3821–3827.

- Byerlee, J. (1978), Friction of rocks, *Pure Appl. Geophys.*, 116, 615–626, doi:10.1007/BF00876528.
- Carslaw, H., and J. Jaeger (1959), *Conduction of Heat in Solids*, vol. 19591, Clarendon Press, Oxford.
- Chester, J. S., F. M. Chester, and A. K. Kronenberg (2005), Fracture surface energy of the Punchbowl fault, San Andreas system, *Nature*, 437(7055), 133–136.
- Di Toro, G., D. L. Goldsby, and T. E. Tullis (2004), Friction falls towards zero in quartz rock as slip velocity approaches seismic rates, *Nature*, 427(6973), 436–439.
- Di Toro, G., T. Hirose, S. Nielsen, G. Pennacchioni, and T. Shimamoto (2006), Natural and experimental evidence of melt lubrication of faults during earthquakes, *Science*, 311(5761), 647–649.
- Di Toro, G. et al. (2010), From field geology to earthquake simulation: A new state-of-the-art tool to investigate rock friction during the seismic cycle (shiva), *Rend. Lincei*, 21(1), 95–114.
- Di Toro, G., R. Han, T. Hirose, N. De Paola, S. Nielsen, K. Mizoguchi, F. Ferri, M. Cocco, and T. Shimamoto (2011), Fault lubrication during earthquakes, *Nature*, 471(7339), 494–498.
- Di Toro, G., S. Mittempergher, F. Ferri, T. M. Mitchell, and G. Pennacchioni (2012), The contribution of structural geology, experimental rock deformation and numerical modelling to an improved understanding of the seismic cycle: Preface to the special volume "Physico-chemical Processes in Seismic Faults", *J. Struct. Geol.*, 38, 3–10.
- Faulkner, D., C. Jackson, R. Lunn, R. Schlische, Z. Shipton, C. Wibberley, and M. Withjack (2010), A review of recent developments concerning the structure, mechanics and fluid flow properties of fault zones, *J. Struct. Geol.*, 32(11), 1557–1575.
- Faulkner, D., T. Mitchell, E. Jensen, and J. Cembrano (2011), Scaling of fault damage zones with displacement and the implications for fault growth processes, *J. Geophys. Res.*, 116, B05403, doi:10.1029/2010JB007788.
- Fondriest, M., S. A. Smith, G. Di Toro, D. Zampieri, and S. Mittempergher (2012), Fault zone structure and seismic slip localization in dolostones, an example from the Southern Alps, Italy, *J. Struct. Geol.*, 45, 52–67.
- Fondriest, M., S. Aretusini, G. Di Toro, and S. A. Smith (2015), Fracturing and rock pulverization along an exhumed seismogenic fault zone in dolostones: The Foiana fault zone (Southern Alps, Italy), *Tectonophysics*, 654, 56–74.
- Fredrich, J. T., and T.-F. Wong (1986), Micromechanics of thermally induced cracking in three crustal rocks, *J. Geophys. Res.*, 91(B12), 12,743–12,764.
- Glover, P., P. Baud, M. Darot, P. Meredith, S. Boon, M. LeRavalec, S. Zoussi, and T. Reuschle (1995),  $\alpha/\beta$  phase transition in quartz monitored using acoustic emissions, *Geophys. J. Int.*, 120(3), 775–782.
- Goldsby, D. L., and T. E. Tullis (2011), Flash heating leads to low frictional strength of crustal rocks at earthquake slip rates, *Science*, 334(6053), 216–218, doi:10.1126/science.1207902.
- Guegen, Y., and V. Palciauskas (1995), Introduction to the physics of rocks, *Phys. Today*, 48(4), 83.
- Han, R., T. Shimamoto, T. Hirose, J.-H. Ree, and J.-i. Ando (2007), Ultralow friction of carbonate faults caused by thermal decomposition, *Science*, 316(5826), 878–881, doi:10.1126/science.1139763.
- Han, R., T. Hirose, and T. Shimamoto (2010), Strong velocity weakening and powder lubrication of simulated carbonate faults at seismic slip rates, *J. Geophys. Res.*, 115, B03412, doi:10.1029/2008JB006136.
- Haskell, N. (1964), Total energy and energy spectral density of elastic wave radiation from propagating faults, *Bull. Seismol. Soc. Am.*, 54(6A), 1811–1841.
- Hirono, T., et al. (2008), Clay mineral reactions caused by frictional heating during an earthquake: An example from the Taiwan Chelungpu fault, *Geophys. Res. Lett.*, 35, L16303, doi:10.1029/2008GL034476.
- Hirose, T., and T. Shimamoto (2005), Growth of molten zone as a mechanism of slip weakening of simulated faults in gabbro during frictional melting, *J. Geophys. Res.*, 110, B05202, doi:10.1029/2004JB003207.
- Kanamori, H., and L. Rivera (2006), Energy partitioning during an earthquake, in *Earthquakes: Radiated Energy and the Physics of Faulting*, *Geophys. Monogr. Ser.*, pp. 3–13, AGU, Washington, D. C., doi:10.1029/170GM03.
- Lachenbruch, A. H., and J. Sass (1992), Heat flow from Cajon pass, fault strength, and tectonic implications, *J. Geophys. Res.*, 97(B4), 4995–5015.
- Ma, K.-F., et al. (2006), Slip zone and energetics of a large earthquake from the Taiwan Chelungpu-fault drilling project, *Nature*, 444(7118), 473–476.
- McGarr, A., J. B. Fletcher, and N. M. Beeler (2004), Attempting to bridge the gap between laboratory and seismic estimates of fracture energy, *Geophys. Res. Lett.*, 31, L14606, doi:10.1029/2004GL020091.
- Mitchell, T., and D. Faulkner (2009), The nature and origin of off-fault damage surrounding strike-slip fault zones with a wide range of displacements: A field study from the Atacama fault system, northern Chile, *J. Struct. Geol.*, 31(8), 802–816.
- Nielsen, S., G. Di Toro, T. Hirose, and T. Shimamoto (2008), Frictional melt and seismic slip, *J. Geophys. Res.*, 113, B01308, doi:10.1029/2007JB005122.
- Nielsen, S., E. Spagnuolo, S. A. F. Smith, M. Violay, G. Di Toro, and A. Bistacchi (2016), Scaling in natural and laboratory earthquakes, *Geophys. Res. Lett.*, 43, 1504–1510, doi:10.1002/2015GL067490.
- Niemeijer, A., G. Di Toro, S. Nielsen, and F. Di Felice (2011), Frictional melting of gabbro under extreme experimental conditions of normal stress, acceleration, and sliding velocity, *J. Geophys. Res.*, 116, B07404, doi:10.1029/2010JB008181.
- Oleskevich, D., R. Hyndman, and K. Wang (1999), The updip and downdip limits to great subduction earthquakes: Thermal and structural models of Cascadia, South Alaska, SW Japan, and Chile, *J. Geophys. Res.*, 104(B7), 14,965–14,991.
- Passelègue, F. X., A. Schubnel, S. Nielsen, H. S. Bhat, and R. Madariaga (2013), From sub-Rayleigh to supershear ruptures during stick-slip experiments on crustal rocks, *Science*, 340(6137), 1208–1211.
- Passelègue, F. X., D. L. Goldsby, and O. Fabbri (2014a), The influence of ambient fault temperature on flash-heating phenomena, *Geophys. Res. Lett.*, 41, 828–835, doi:10.1002/2013GL058374.
- Passelègue, F. X., O. Fabbri, M. Dubois, and S. Ventelon (2014b), Fluid overpressure along an oligocene out-of-sequence thrust in the Shimanto Belt, SW Japan, *J. Asian Earth Sci.*, 86, 12–24.
- Passelègue, F. X., A. Schubnel, S. Nielsen, H. S. Bhat, D. Deldicque, and R. Madariaga (2016), Dynamic rupture processes inferred from laboratory microearthquakes, *J. Geophys. Res. Solid Earth*, 121, 4343–4365, doi:10.1002/2015JB012694.
- Pec, M., H. Stünitz, R. Heilbronner, M. Drury, and C. de Capitani (2012), Origin of pseudotachylites in slow creep experiments, *Earth and Planet. Sci. Lett.*, 355, 299–310.
- Pittarello, L., G. Di Toro, A. Bizzarri, G. Pennacchioni, J. Hadizadeh, and M. Cocco (2008), Energy partitioning during seismic slip in pseudotachylite-bearing faults (Gole Larghe fault, Adamello, Italy), *Earth and Planet. Sci. Lett.*, 269(1), 131–139.
- Reches, Z., and D. A. Lockner (2010), Fault weakening and earthquake instability by powder lubrication, *Nature*, 467(7314), 452–455.
- Rempel, A. W., and S. L. Weaver (2008), A model for flash weakening by asperity melting during high-speed earthquake slip, *J. Geophys. Res.*, 113, B11308, doi:10.1029/2008JB005649.

- Rice, J. R. (2006), Heating and weakening of faults during earthquake slip, *J. Geophys. Res.*, **111**, B05311, doi:10.1029/2005JB004006.
- Scholz, C. H. (2002), *The Mechanics of Earthquakes and Faulting*, Cambridge Univ. Press, Cambridge, U. K.
- Shipton, Z. K., A. M. Soden, J. D. Kirkpatrick, A. M. Bright, and R. J. Lunn (2006), How thick is a fault? Fault displacement-thickness scaling revisited, in *Earthquakes: Radiated Energy and the Physics of Faulting*, *Geophys. Monogr. Ser.*, vol. 170, edited by R. E. Abercrombie et al., pp. 193–198, AGU, Washington, D. C.
- Sibson, R. H. (1975), Generation of pseudotachylite by ancient seismic faulting, *Geophys. J. Int.*, **43**(3), 775–794.
- Spray, J. G. (1995), Pseudotachylite controversy: Fact or friction?, *Geology*, **23**(12), 1119–1122.
- Tanikawa, W., M. Sakaguchi, O. Tada, and T. Hirose (2010), Influence of fault slip rate on shear-induced permeability, *J. Geophys. Res.*, **115**, B07412, doi:10.1029/2009JB007013.
- Tinti, E., P. Spudich, and M. Cocco (2005), Earthquake fracture energy inferred from kinematic rupture models on extended faults, *J. Geophys. Res.*, **110**, B12303, doi:10.1029/2005JB003644.
- Tinti, E., M. Cocco, E. Fukuyama, and A. Piatanesi (2009), Dependence of slip weakening distance ( $D_c$ ) on final slip during dynamic rupture of earthquakes, *Geophys. J. Int.*, **177**(3), 1205–1220.
- Tsutsumi, A., and T. Shimamoto (1997), High-velocity frictional properties of gabbro, *Geophys. Res. Lett.*, **24**(6), 699–702.
- Venkataraman, A., and H. Kanamori (2004), Observational constraints on the fracture energy of subduction zone earthquakes, *J. Geophys. Res.*, **109**, B05302, doi:10.1029/2003JB002549.
- Violay, M., S. Nielsen, E. Spagnuolo, D. Cinti, G. Di Toro, and G. Di Stefano (2013), Pore fluid in experimental calcite-bearing faults: Abrupt weakening and geochemical signature of co-seismic processes, *Earth Planet. Sci. Lett.*, **361**, 74–84.
- Violay, M., S. Nielsen, B. Gibert, E. Spagnuolo, A. Cavallo, P. Azais, S. Vinciguerra, and G. Di Toro (2014), Effect of water on the frictional behavior of cohesive rocks during earthquakes, *Geology*, **42**(1), 27–30.
- Violay, M., G. Di Toro, S. Nielsen, E. Spagnuolo, and J. Burg (2015), Thermo-mechanical pressurization of experimental faults in cohesive rocks during seismic slip, *Earth Planet. Sci. Lett.*, **429**, 1–10.
- Walsh, J. (1965), The effect of cracks on the uniaxial elastic compression of rocks, *J. Geophys. Res.*, **70**(2), 399–411.
- Wang, X.-Q., A. Schubnel, J. Fortin, Y. Guéguen, and H.-K. Ge (2013), Physical properties and brittle strength of thermally cracked granite under confinement, *J. Geophys. Res. Solid Earth*, **118**(12), 6099–6112.
- Wong, T.-f. (1982), Shear fracture energy of Westerly granite from failure behavior, *J. Geophys. Res.*, **87**(B2), 990–1000.